Engineering Failure Analysis 182 (2025) 110070

Contents lists available at ScienceDirect

Engineering Failure Analysis

journal homepage: www.elsevier.com/locate/engfailanal

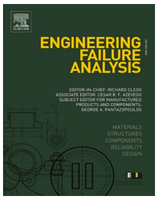

Numerical and analytical modelling of masonry walls failure under waterborne debris impacts

Alessandro De Iasio [a,*], Riccardo Briganti [a], Gabriele Milani [b], Bahman Ghiassi [c]

[a] Faculty of Engineering, University of Nottingham, Nottingham NG7 2RD, UK
[b] Department of Architecture Built Environment and Construction Engineering (ABC), Politecnico di Milano, Piazza Leonardo da Vinci 32, 20133 Milan, Italy
[c] School of Engineering, University of Birmingham, Birmingham B15 2TT, UK

ARTICLE INFO

Keywords:
Waterborne debris impacts
Flood
Structural failure
Masonry
Impulse-momentum theorem
Climate change
Numerical simulation

ABSTRACT

Masonry walls are highly vulnerable to waterborne debris impact loads occurring during extreme hydrodynamic events. These loads are usually represented with a force–time (F-t) diagram calculated using analytical models. Such models are currently derived from elastic structures, neglecting the effects of potential failure mechanisms activated by the impact. At the same time, current design standards lack design prescriptions that consider structural failure in debris impact design. To address this gap, the present paper investigates the effects of structural failure on F-t diagrams and proposes a new model, the Energy and Impulse-Momentum Model (EIMM), to compute analytical nonlinear F-t diagrams that account for such structural nonlinearities. The focus is on masonry structures due to their popularity in the built environment, but the findings can be extended to any impact scenario. It is shown that structural failure significantly reduces the impact force due to the decrease in structural stiffness. A Performance Index, PI, is used to quantify this reduction and is proposed as a potential design parameter. It is also shown that the proposed EIMM can effectively compute nonlinear analytical F-t diagrams. The results of this research deliver new knowledge and methods for debris impact design of nonlinear structures needed to guarantee public technical safety of structures in extreme hydrodynamic events.

1. Introduction

Waterborne debris impacts in extreme hydrodynamic events are high-magnitude impulsive loads that can affect structural integrity [1]. Under the changing climate and the expected increase in both the intensity and frequency of such events, it is critical to reliably assess the resilience of existing structures under these loading scenarios.

The magnitude of waterborne debris impacts depends on the debris-structure interaction: the debris contributes with its hammering action while the structure resists it. These actions are commonly characterised by analytical debris impact Force-time (F-t)

---

* Corresponding author.
E-mail addresses: alessandro.deiasio@nottingham.ac.uk (A. De Iasio), riccardo.briganti@nottingham.ac.uk (R. Briganti), gabriele.milani@polimi.it (G. Milani), b.ghiassi@bham.ac.uk (B. Ghiassi).

https://doi.org/10.1016/j.engfailanal.2025.110070
Received 1 August 2025; Received in revised form 28 August 2025; Accepted 29 August 2025

Nomenclature

A_d	Log debris cross-section area
A_{impact}	Impact area
C_p	Pressure water flow coefficient
DIF	Dynamic Increase Factor
d	Ductility parameter
δ	Stiffness ratio
E	Energy quantity for solid debris impact models
$\widetilde{E}$	Energy quantity for equivalent force impact models
E_d	Debris Young's modulus
E_s	Structure Young's modulus
$\in$	Eccentricity parameter
ε	Strain
$\dot{\varepsilon}$	Strain rate
ε_t^{ck}	Tensile cracking strain
$\widetilde{\varepsilon}_t^{pl}$	Tensile equivalent plastic strain
η	Viscosity parameter
F	Debris impact force
Fr	Froude number
φ_d	Log debris cross-section diameter
g	Gravity acceleration
G_f^t	Tensile fracture energy
G_f^c	Compressive fracture energy
γ	Generic error quantity
h_w	Water depth
H	Target function solved by the EIMM
I	Impulse of the F-t diagram
l_{ec}	Finite element characteristic length
K_c	Ratio of the biaxial to uniaxial compressive yield stresses
k_d	Debris stiffness
k_s	Structure stiffness
L_d	Debris length
λ	Scaling factor
m_d	Debris weight
μ	Mass ratio
ν	Poisson's ratio
p	Vertical loads
PI	Performance Index
ψ	Dilation angle
q_{hd}	Hydrodynamic pressure
q_{hs}	Hydrostatic pressure
q_w	Water flow pressure
ρ	Material density
ρ_w	Fluid density
ρ_d	Debris density
s	Mesh size
SW	Structural self-weight
σ	Stress
σ_{b0}	Biaxial compressive yield stress
σ_c	Uniaxial compressive strength
σ_{c0}	Uniaxial compressive yield stress
σ_t	Uniaxial tensile strength
t	Simulation physical time
t_d	Debris impact duration
u	Structural horizontal displacement
v_d	Debris velocity
v_w	Flow velocity
w	Crack width

diagrams. Existing analytical models, including those proposed in ASCE/SEI 7-22 [2], assume elastic debris-structure interactions, i.e. debris and structure behave elastically during the impact. However, post-disaster surveys indicate that structures often exhibit nonlinear behaviour under debris impacts as failure mechanisms are activated. This particularly occurs for low-tensile strength structures like masonry [3,4]. While there are already a few studies on incorporating debris nonlinearities in calculating debris impact forces on elastic structures [5], there is a lack of knowledge on the role of structural failure on these forces.

To address this gap, the present study investigates the influence of structural failure on the F-t diagram of waterborne log debris impacts on masonry structures and proposes a novel analytical method, the Energy and Impulse-Momentum Model (EIMM), to compute the associated analytical nonlinear F-t diagrams. The generalisation of the presented findings to other structures and debris types is discussed. These research objectives are achieved by carrying out numerical simulations with the commercial software Abaqus/CAE [6]. The influence of structural failure is assessed through high-fidelity impact simulations, comparing impact force histories on elastic and nonlinear structures across various scenarios involving different debris and structure properties, vertical loads, and water flow loads. The EIMM has finally been developed using these high-fidelity numerical data as a reference. The results of this research deliver new knowledge and methods for debris impact design of nonlinear structures needed to guarantee public technical safety of structures in extreme hydrodynamic events.

2. Structural model

Debris impacts on masonry walls are numerically simulated with explicit Finite Element models using the commercial code Abaqus [6]. The analysed structure is a nonlinear masonry wall (Section 2.1). The debris is assumed to behave elastically to exclude the effects of debris nonlinearities [5], thus isolating those of structural nonlinearities. The cases with both nonlinear debris and structures are out of the scope of this study, and their investigation is postponed to future research. The debris and the other acting loads are defined in Section 2.2.

2.1. Masonry wall

The masonry wall analysed is a rectangular running-bond clay brick wall with no openings. This wall is $5.615m$ wide, $2.475m$ tall and $0.1025m$ thick, with $215\times102.5\times65mm^3$ bricks and $10mm$ thick 1:1:6 (cement:lime:sand) mortar layers. The wall has a fixed base, supported vertical edges and a free top edge. A masonry micro model is used, where bricks and mortar are connected by tied interfaces (Fig. 1-a). Mesh consists of linear hexahedral elements (C3D8), with a size s of $35mm$. Mortar layers, however, contain only one element across their thickness, leading to a smaller mesh size in that direction. Mesh nodes are set to coincide at the interfaces to merge brick and mortar meshes and reduce computational costs.

This micro model is validated by [7] against experimental tests by [8] performed on different masonry walls under out-of-plane loads. The validation is carried out for two different walls, i.e. the one described above and used in this study, and one with openings. Results showed strong agreement between numerical and experimental data in terms of both structural behaviour and failure modes. Strong agreements were also identified against other numerical results [9,10] simulating the same experimental tests. Therefore, this micro model is suitable to analyse the structural behaviour of masonry walls under out-of-plane loads.

Materials are homogeneous with density ρ, Young's modulus E and Poisson's ratio ν. Materials nonlinearity is modelled with the Concrete Damage Plasticity (CDP) model [6], as common for masonry models [11]. Uniaxial compressive and tensile post-elastic stress–strain ($\sigma - \varepsilon$) curves are defined. The compressive curve is [12]:

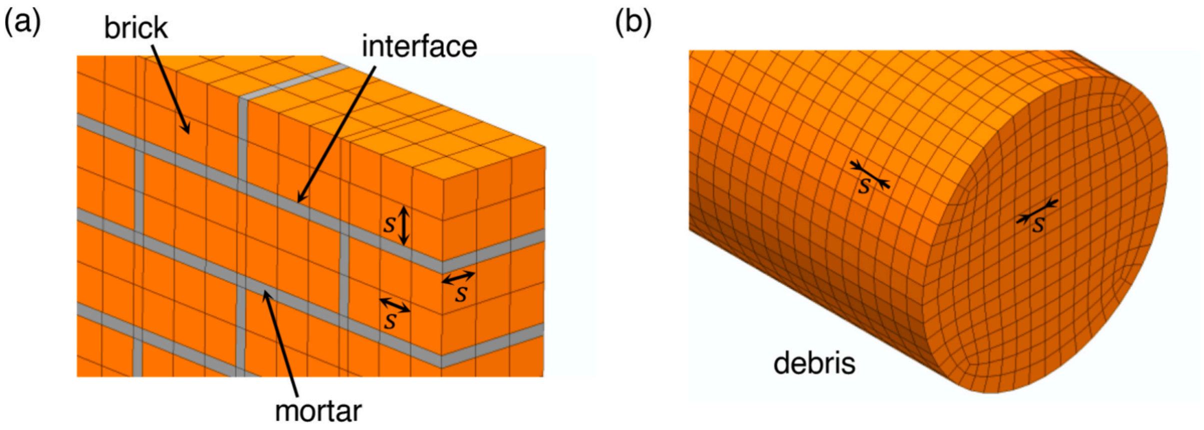

Fig. 1. (a) Micro-model and mesh layout for the masonry wall. (b) Debris mesh layout.

$$\sigma(\varepsilon) = \begin{cases} \frac{\sigma_c}{3}\left(1 + 4\left(\frac{\varepsilon - \varepsilon_{c,3}}{\varepsilon_c - \varepsilon_{c,3}}\right) - 2\left(\frac{\varepsilon - \varepsilon_{c,3}}{\varepsilon_c - \varepsilon_{c,3}}\right)^2\right), & \varepsilon_{c,3} \le \varepsilon < \varepsilon_c \\ \frac{\sigma_c}{3}\left(1 - \left(\frac{\varepsilon - \varepsilon_c}{\varepsilon_u - \varepsilon_c}\right)^2\right), & \varepsilon_c \le \varepsilon < \varepsilon_u \\ 0, & \varepsilon \ge \varepsilon_u \end{cases} \tag{1}$$

with yielding strain $\varepsilon_{c,3} = \sigma_c/(3E)$, strain at peak strength $\varepsilon_c = 5\sigma_c/(3E)$, ultimate strain $\varepsilon_u = \varepsilon_c + 3G_f^c/(2l_{ec}\sigma_c)$, compressive strength σ_c and compressive fracture energy G_f^c. The equivalent element length l_{ec} allows for a mesh-independent post-elastic response and is equal to the element volume divided by its largest face area [13]. Instead, the tensile curve is [14]:

$$\sigma(w) = \sigma_t\left\{\left[1 + \left(c_1\frac{w}{w_c}\right)^3\right]e^{-c_2\frac{w}{w_c}} - \frac{w}{w_c}(1 + c_1^3)e^{-c_2}\right\} \tag{2}$$

with tensile strength σ_t, crack width w, coefficients $c_1 = 3$ and $c_2 = 6.93$ and ultimate crack width $w_c = 5.14\ G_f^t/\sigma_t$, where G_f^t is the tensile fracture energy. Bricks and mortar parameters are in Table 1. Across the text, subscripts "b" and "m" are used to refer to bricks and mortar properties.

The CDP plasticity parameters are defined as in [7]. These include dilation angle ψ, eccentricity parameter $\in$, ratio of the biaxial to uniaxial compressive yield stresses σ_{bo}/σ_{c0}, ratio between the second stress invariant on the tensile meridian to that on the compressive meridian K_c and viscosity parameter η. Default values are used for $\in$, σ_{bo}/σ_{c0}, K_c and η, i.e. 0.1, 1.16, 0.667 and 0. The angle ψ_b is equal to 35°, while ψ_m is set by following [15] to replicate shear failures at bed joints under vertical stresses. Self-weight causes low vertical stresses associated with $\psi_m = 43^\circ$, while $\psi = 10^\circ$ is required when higher vertical loads are present.

High strain rate effects are modelled by multiplying material properties by the Dynamic Increase Factors (DIF) function of the strain rate $\dot{\varepsilon}$. This $\dot{\varepsilon}$ dependency is modelled with a user-defined Fortran subroutine proposed by [7]. DIF are applied only to σ_t and G_f^t as the most influential dynamic properties in these scenarios [7]. The DIF equation for bricks and mortar are [16]:

$$DIF_b = \begin{cases} 0.0268\ln(\dot{\varepsilon}) + 1.3504, & 2\ 10^{-6}s^{-1} < \dot{\varepsilon} < 3.2s^{-1} \\ 0.2405\ln(\dot{\varepsilon}) + 1.1041, & 3.2s^{-1} < \dot{\varepsilon} < 150s^{-1} \end{cases} \tag{3}$$

$$DIF_m = \begin{cases} 0.0372\ln(\dot{\varepsilon}) + 1.4025, & 2\ 10^{-5}s^{-1} < \dot{\varepsilon} < 13s^{-1} \\ 0.3447\ln(\dot{\varepsilon}) + 0.5987, & 13s^{-1} < \dot{\varepsilon} < 200s^{-1} \end{cases} \tag{4}$$

2.2. Acting loads

The impact scenario is waterborne log debris impacting a masonry wall in an extreme hydrodynamic event (Fig. 2-a). The flow has velocity v_w and depth h_w. The debris is driven with uniform motion until it hits the structure at midspan with velocity v_d equal to v_w [17–19] and height equal to h_w. The log is assumed to impact the wall orthogonally to maximise peak impact force [20,21]. The debris force is introduced in two different forms following two different modelling strategies: the solid debris impact model (Fig. 2-c) and the equivalent impact force model (Fig. 2-d). In the solid debris impact model, the debris-structure interaction is explicitly modelled by representing the debris hitting the structure. In contrast, the equivalent impact force model simplifies the mechanical system by introducing the impact force with an equivalent F-t diagram. The solid model accurately simulates the debris-structure interaction [22]. Therefore, it is used to analyse the effects of structural nonlinearities on the debris impact force and provides the reference data to develop the proposed analytical model that integrates structural nonlinearities. Instead, the equivalent model is the current practice for existing research and design, and is used in this study to evaluate the structural behaviour under F-t diagrams calculated a priori, e.g., with the analytical model proposed in this research.

In the solid debris impact model, the log representing debris is meshed with linear hexahedral elements (C3D8) and $s = 20mm$ (Fig. 1-b), following [23], which shows that s ranging from $5mm$ to $30mm$ lead to mesh independent results with the same element types. The debris-structure contact is modelled with the General Contact algorithm based on contact penalty [6]. The contact friction coefficient is set to 0.50 as typical of wood against masonry to represent realistic interactions [24]. No damping is implemented as it does not influence the peak structural responses such as maximum displacements under impact loads [25]. The impact force F is the total force at the debris-structure contact area in time t and the value of $F(t)$ defines the numerical F-t diagrams.

In the equivalent force impact model, the impact F-t diagram is implemented as a uniform pressure with total force equal to $F(t)$ on

Table 1
Mechanical properties of bricks and mortar [7].

	ρ[kg/m^3]	E[MPa]	ν[-]	σ_c[MPa]	G_f^c[N/m]	σ_t[MPa]	G_f^t[N/m]
Bricks	1590	16,700	0.20	38.20	38,200	3.82	64
Mortar	2113	4000	0.20	11.50	11,500	0.58	28

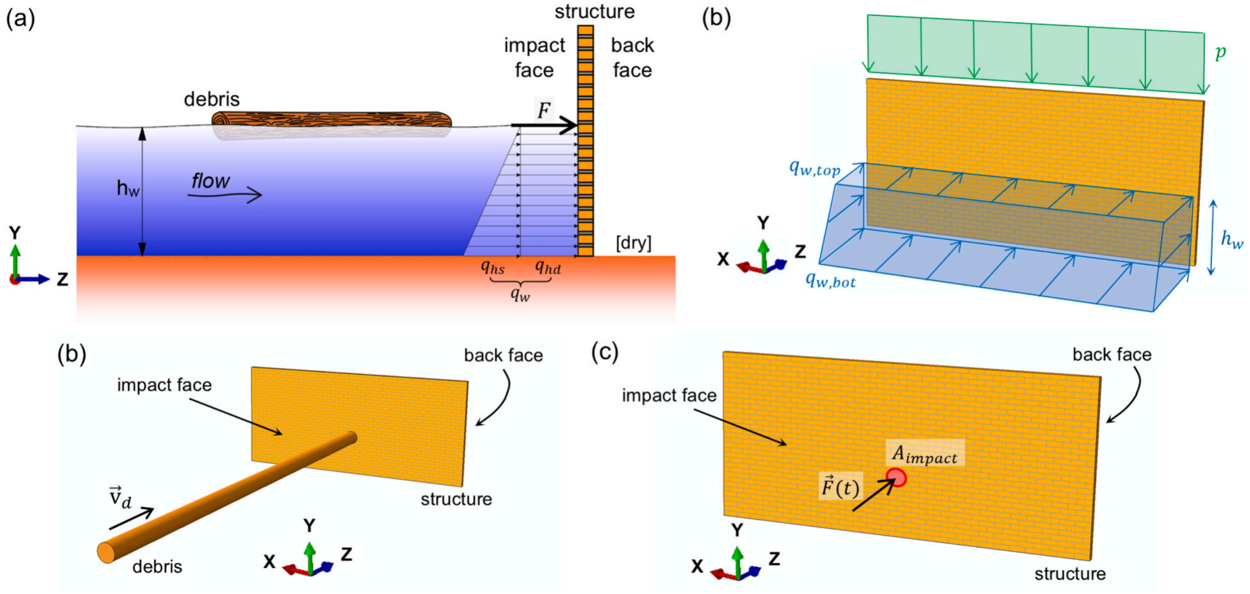

Fig. 2. (a) Impact scenario, (b) solid debris impact model and (c) equivalent impact force model.

an impact area A_{impact} equal to A_d. The F-t diagram can be defined in two ways. First, using analytical models, which lead to a simulations reliability depending on the accuracy of the applied F-t diagram. Second, using the high-fidelity numerical simulations carried out with the related solid debris impact model, i.e. the one representing the same impact scenario. In this latter case, the applied F-t diagram is defined as the *actual* F-t diagram, and the equivalent force impact model using such a diagram is defined as the *actual* equivalent model.

The debris properties are set as the minimum design parameter by ASCE/SEI 7–22 for log debris. These properties are $m_d = 454kg$ and $k_d = 61300kN/m$, which corresponds to a length of $L_d = 9m$, a diameter of $\varphi_d = 0.305m$, $E_d = 7550MPa$ and $\rho_d = 690.4kg/m^3$. Note that k_d is the axial log stiffness calculated as $k_d = E_d A_d / L_d$, with A_d being the debris cross-section. The Poisson's ratio ν_d is set to 0.3 as typical for wood [26].

In addition to the debris impact, the following loads also act on the structure. The structural self-weight, SW, and the vertical top load p act in the vertical direction (Fig. 2-b). Note that p represents the gravity loads introduced to walls in typical two-storey buildings considering two scenarios of $p_1 = 13.19kN/m$ and $p_2 = 37.76kN/m$ [27]. Moreover, the water flow pressure q_w acts horizontally over the wall wet surface. This load, computed assuming a steady state flow as in existing literature, is the sum of a triangular hydrostatic pressure q_{hs} and uniform hydrodynamic pressure q_{hd} [27,28]. The load q_{hs} is calculated as $q_{hs} = \rho_w g h_w$, where ρ_w is the fluid density set to $1100kg/m^3$ to consider water with entrapped sediments [2]. The load q_{hd} is calculated as $q_{hd} = 0.5\rho_w C_p v_w^2$, where C_p is the pressure coefficient set to 1.5 [27]. It follows that q_w is a trapezoidal pressure with top value $q_{w,top} = q_{hd}$ and bottom value $q_{w,bot} = q_{hd} + q_{hs}$. The Froude number $Fr = v_w / \sqrt{g h_{h_w}}$, with g being the gravity acceleration, links v_w and h_w. A subcritical flow, $Fr = 0.6$, is assumed as a common realistic condition [28]. The value of h_w is set equal to $0.9m$ as the minimum water depth to consider debris floating by ASCE/SEI 7-22. This leads to $v_w = 1.78m/s$. Using the selected values for h_w and v_w, $q_{hs} = 9.71kPa$ and $q_{hd} = 2.62kPa$, leading to $q_{w,top} = 2.62kPa$ and $q_{w,bot} = 12.33kPa$. In summary, three load cases are considered, namely only-debris, $SW + p$ and $SW + q_w$. The only-debris case aligns with ASCE/SEI 7-22, in which debris impacts are not combined with other loads. The $SW + p$ and $SW + q_w$ cases consider the contribution of SW, p and q_w in addition to the debris load. Therefore, comparing these results with the only-debris load case allows to highlight the effects of such loads. Remembering that two values of p are defined, the related load cases are $SW + p_1$ and $SW + p_2$.

3. Numerical investigations

3.1. Simulations programme

The importance of structural nonlinearities is investigated through high-fidelity simulations carried out using solid debris impact models (Fig. 2-c) on a masonry wall defined in Section 2.1 and load cases introduced in Section 2.2. Numerical nonlinear F-t diagrams are extracted from the results. The role of structural nonlinearities is identified by comparing these diagrams to numerical elastic F-t diagrams. Numerical elastic diagrams are obtained by implementing only the elastic material properties for the studied structure. The nonlinear and elastic F-t diagrams are compared in two steps. First, qualitative discussions examine the characteristics of the nonlinear diagrams relative to the elastic ones. Second, such diagrams are quantitatively compared as a whole using the Performance Index PI, calculated as:

$$PI = \frac{I_{nonlinear}}{I_{elastic}} \tag{5}$$

where $I_{nonlinear}$ and $I_{elastic}$ are the impulses of the nonlinear and elastic F-t diagrams, respectively. The value of PI is less than or equal to 1 and conveys the *performance* of a structure in resisting debris impacts. The impulse I is calculated as:

$$I = \int_0^{t_d} F(t)dt \tag{6}$$

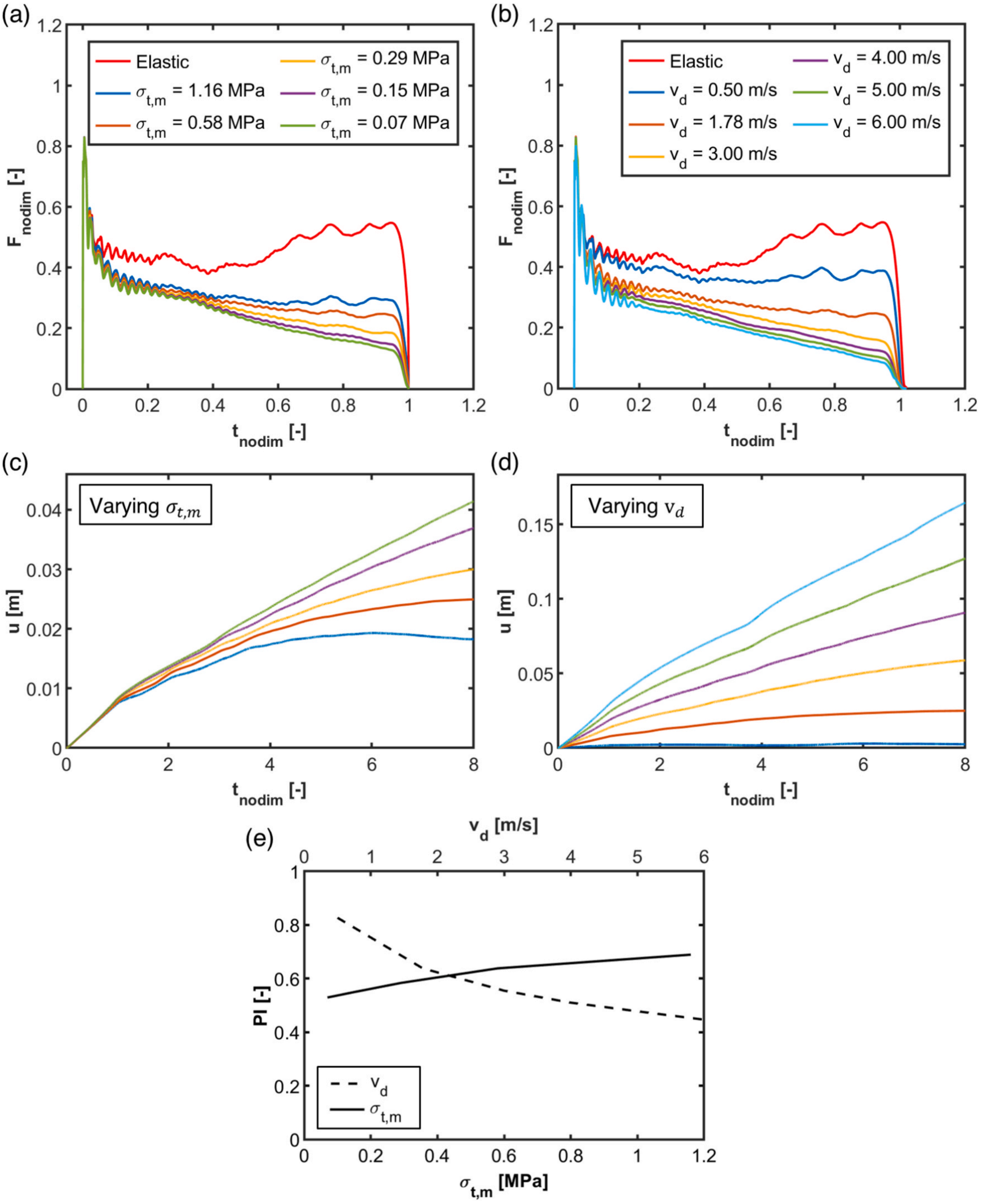

Fig. 3. Varying $\sigma_{t,m}$ and v_d, (a, b) elastic and nonlinear numerical F-t diagrams, (c, d) u and (e) PI.

To facilitate data discussion, nondimensional F-t diagrams are presented using F_{nodim} and t_{nodim}, calculated as:

$$F_{nodim} = \frac{F}{\mathrm{v}_d\sqrt{m_d k_d}}, \qquad t_{nodim} = \frac{t}{2\sqrt{m_d/k_d}} \tag{7}$$

The horizontal structural displacements u of nonlinear and elastic simulations are also compared to support the discussion on the effects of structural nonlinearities. Such displacements are discussed in terms of both their whole time-history and maximum value u_{max}. The displacement control point is on the wall surface opposite the impact surface and in correspondence with the impact area centroid.

A broad overview of the effects of structural nonlinearities is obtained by analysing different load cases in different impact scenarios. These scenarios are defined by varying v_d and $\sigma_{t,m}$ starting from the baseline values $\sigma_{t,m} = 0.58MPa$ and $\mathrm{v}_d = 1.78m/s$ (see Sections 2.1 and 2.2, respectively). These analyses allow for overlooking the influence of different loads, structural damage, and impact severity and generalise the results. For this, v_d values of 0.5, 3, 4, 5 and $6m/s$, which are among the impact velocities tested by Piran Aghl et al. (2014), and $\sigma_{t,m}$ values of 1.16, 0.29, 0.15 and $0.07MPa$, which are common mortar tensile strengths [11] are considered. These values represent 100%, 50%, 25% and 12.5% of the baseline value, also leading to variable G_f^t (as for Section 2.1) with the same factors. This broad range of $\sigma_{t,m}$ allows to effectively study weakening structures under the influence of mortar failure. The baseline values of $\sigma_{t,m}$ and v_d are used when varying v_d and $\sigma_{t,m}$, respectively.

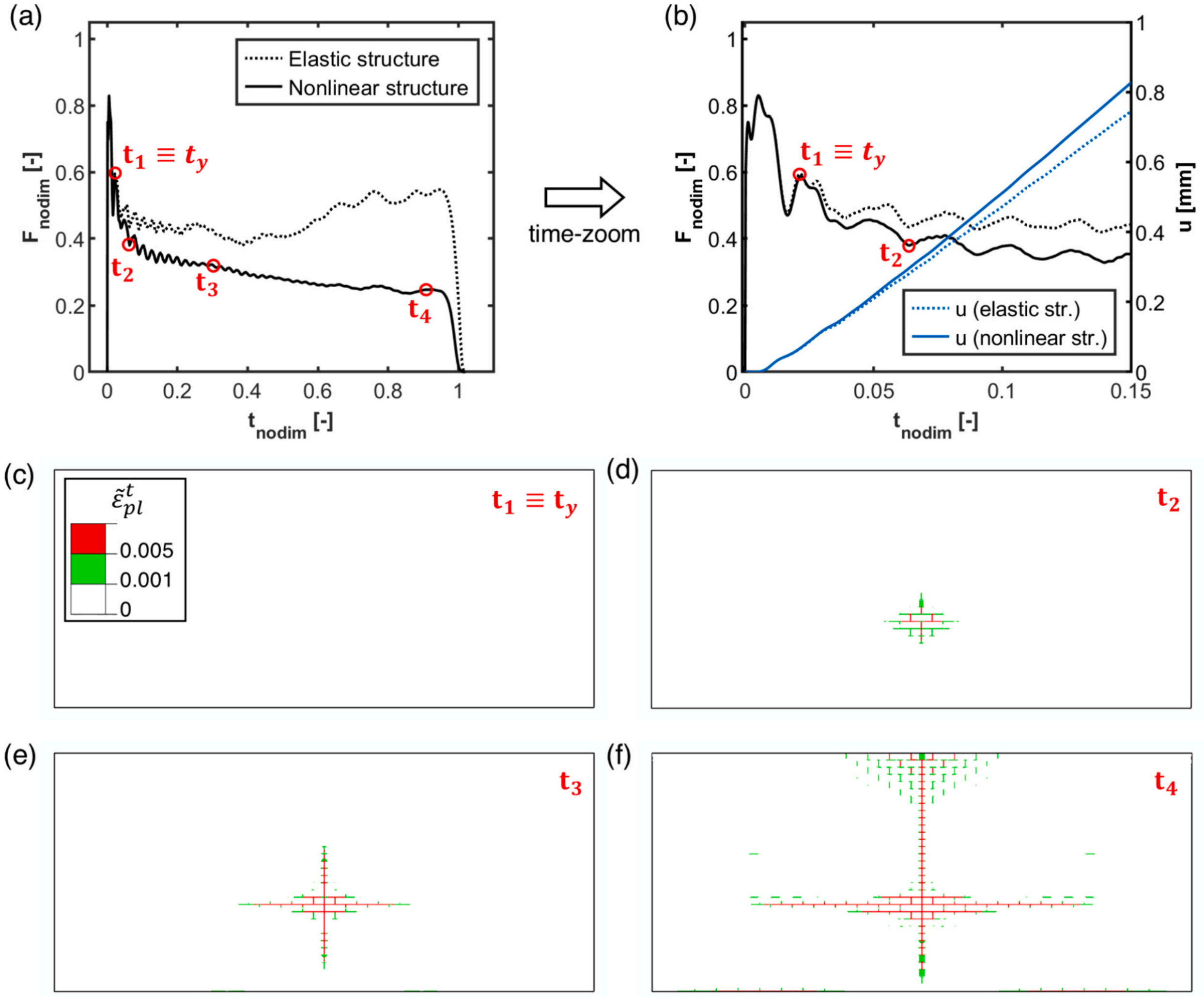

Fig. 4. (a) Full and (b) time-zoomed numerical elastic and nonlinear F-t diagrams. Crack patterns at (c) $t_1 \equiv t_y$, (d) t_2, (e) t_3 and (f) t_4.

3.2. Only-debris load case

The numerical nonlinear F-t diagrams obtained from the solid debris impact model are shown in Fig. 3-a, b as a function of $\sigma_{t,m}$ and v_d. The related numerical elastic diagrams are also shown for comparison. Note that the nondimensional elastic diagrams for varying v_d coincide since results are normalised with respect to v_d in lieu of Eq. (7). These analyses are obtained excluding the high-strain rate effects in the material model to reduce the parameters potentially influencing the results. The influence of high-strain rate effects is specifically investigated in Section 3.4.

Fig. 3-a, b show that the impact force of nonlinear F-t diagrams is lower than that of related elastic diagrams. Moreover, nonlinear diagrams have lower force values as $\sigma_{t,m}$ decreases and as v_d increases. This is due to the structural damage, which reduces the structural stiffness and, in turn, the impact force. Such a reduction is also observed in elastic impacts where impact forces decrease with structural stiffness [20]. Displacements also significantly increase as $\sigma_{t,m}$ decreases and as v_d increases (Fig. 3-c,d), which is expected given the increased structural damage. Moreover, *PI* (Eq. (5) is always lower than 1 (Fig. 3-e) and a relationship between *PI*, and $\sigma_{t,m}$ and v_d can be observed. In general, the impact force and the structural resistance are directly proportional, and the structural resistance is given by the inertia forces and structural stiffness [20,22]. It is observed that *PI* decreases at a lower rate as v_d increases than when $\sigma_{t,m}$ decreases. This is because, while the structural stiffness decreases as v_d increases due to the higher damage caused by the impact action, the structural resistance is governed by the inertia forces, which increase with increasing v_d due to activation of higher structural accelerations.

Nonlinear F-t diagrams and related structural displacements for the case of $\sigma_{t,m} = 0.58MPa$ and $v_d = 1.78m/s$ are presented in Fig. 4. Damage is shown with crack patterns on the back face of the wall (Fig. 2-a) at meaningful times (Fig. 4-a) in terms of equivalent plastic tensile strain $\widetilde{\varepsilon}_t^{pl}$, which is the CDP hardening variable in tension [6]. This strategy follows [7], who proposed 0.001 and 0.005 as $\widetilde{\varepsilon}_t^{pl}$ contour thresholds, which correspond to 30 % and 70 % reduction for mortar peak strength, and 60 % and 98 % of brick peak strength. These values effectively convey structural damage in bricks and mortar layers. It can be observed that the elastic and nonlinear F-t diagrams coincide until t_1 (Fig. 4-b). Comparing the displacement u of the cases with elastic and nonlinear structures, these also diverge at t_1. Therefore, t_1 is identified as the time at which structural nonlinearities arise and referred to as the yielding time

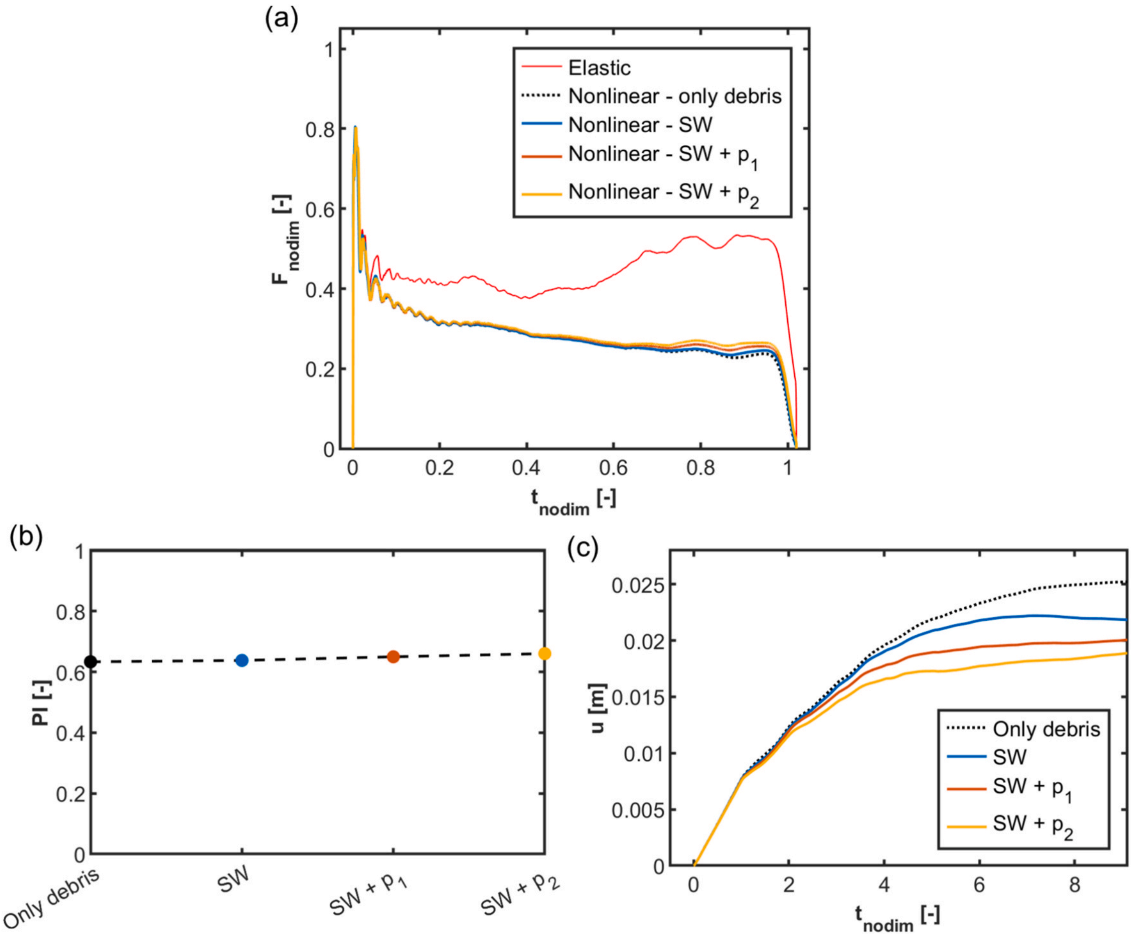

Fig. 5. Simulations for load cases $SW + p$: (a) numerical F-t diagrams, (b) *PI* and (c) u.

t_y. Crack patterns show that no damage occurs for $t < t_y$ (Fig. 4-c) and that the difference between the elastic and nonlinear outputs increases as structural damage progresses when $t \geq t_y$ (Fig. 4-d,e,f). These data on F-t diagrams, structural displacements and crack patterns show the governing role of structural damage in the nonlinear debris-structure interactions.

It is worth noting the similarities of the presented results with the earthquake engineering practice, where the elastic seismic response spectrum is scaled to account for the structural nonlinear behaviour. This scaling is performed through the behaviour factor q (or force modification factor R), which enables the carrying out of elastic analyses in place of inelastic ones. The q-factor depends on the structural typology, structural systems and building materials [29]. Its value is directly proportional to the expected structural ductility under the earthquake action [25]. Similarly, in debris impact problems, the nonlinear F-t diagrams can be reduced with respect to the elastic one with PI as the quantifying parameter for this reduction. Therefore, PI can be used as a design parameter in a performance-based debris impact design. The acceptable threshold values of PI for each design limit state require further investigations and should be defined in future research.

While fully coupled debris and structure nonlinearities should be investigated in future research, the presented results show the accuracy of the assumption of debris behaving elastically (see Section 2). Indeed, the maximum force is $F \cong 800kN$ (from Eq. (7) for $v_d = 6m/s$), which corresponds to $\cong 11MPa$ compressive stress on A_d and is lower than common wood strength, i.e. 30 $-50MPa$ [26]. Moreover, despite referring to specific debris and structural properties, the presented results can be generalised in lieu of the clear causation between the impact force reduction and structural damage. Therefore, these findings can be extended to various impact scenarios with different debris types, e.g. cars, and different masonry structures and other nonlinear structures. Common variations of the presented structural set-up would include the presence of openings in the wall. This presence would have the same effects as that of

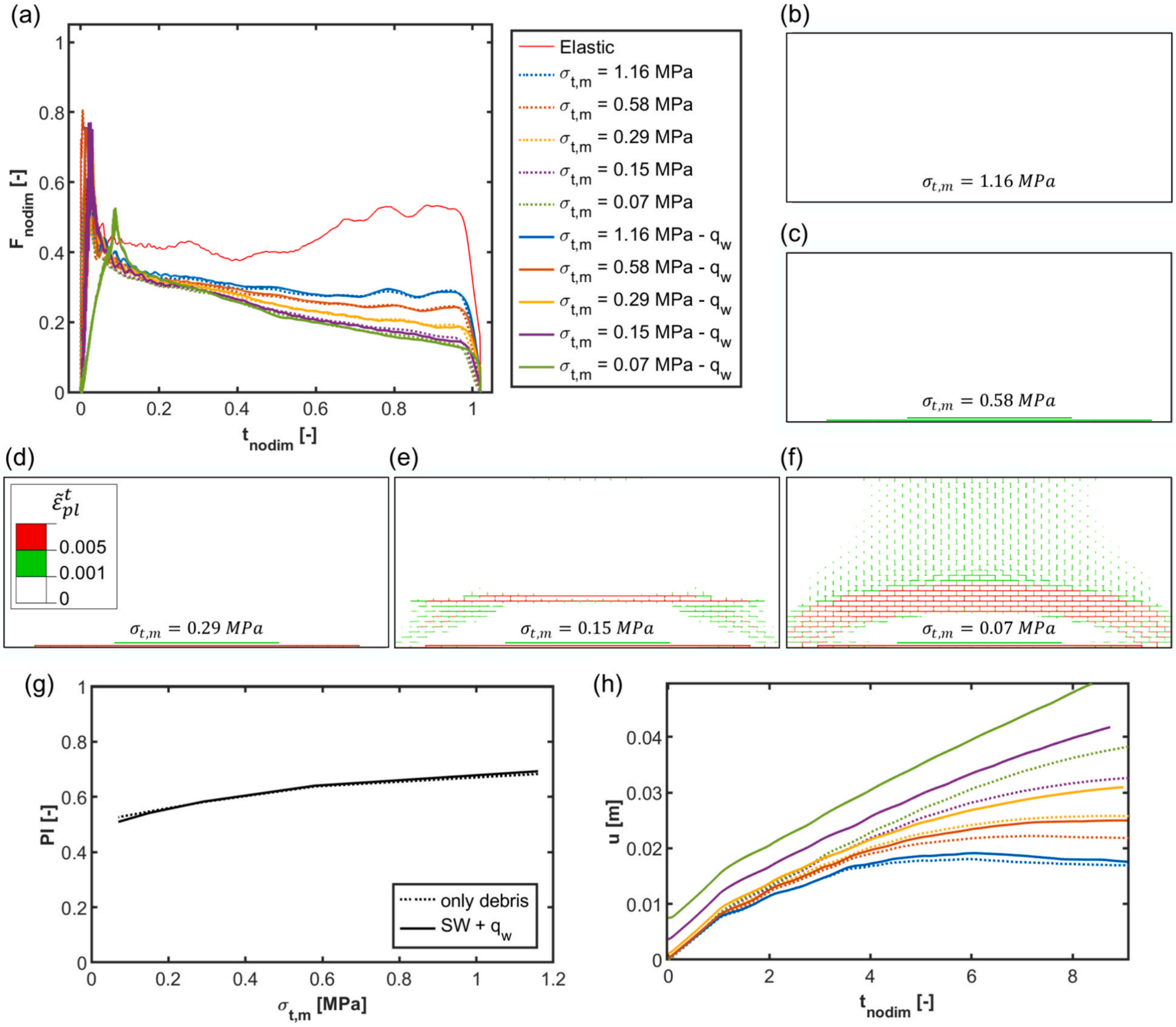

Fig. 6. Results of load cases $SW + q_w$ and different $\sigma_{t,m}$: (a) numerical F-t diagrams, pre-impact damage caused by q_w for (b) $\sigma_{t,m} = 1.16$, (c) 0.58, (d) 0.29, (e) 0.15 and (f) 0.07 MPa, (g) PI and (h) u.

weaker material strengths, as shown in this section. Indeed, wall openings would decrease the structural capacity [8] and consequently lead towards a lower impact force and *PI* compared to the case with no openings. Moreover, the indirect proportionality between structural capacity and opening ratio [8] conveys that the *PI* would decrease as the opening ratio increases. Another possible structure variation is in terms of boundary conditions. In general, boundary conditions influence the structural stiffness and failure modes [9]. Structural stiffness is also proportional to the debris impact force [20]. Therefore, changing boundary conditions, e.g. pinning the wall at the four sides, would modify, first, the related elastic impact force, and, second, the failure mode. Nevertheless, the wall failure would still proportionally decrease the impact force and *PI* in line with the results of this section. However, given the intrinsic nonlinearity of this problem, each debris-structure combination is expected to have specific parameters and key failure mechanisms that govern the nonlinear debris-structure interaction. These specifics must be identified in dedicated future studies to assess the most critical structural configurations for debris impacts..

3.3. Effects of vertical and horizontal loads

The results of the load cases $SW+p$ alongside with those of the only-debris load case are presented in this section. Fig. 5-a and b show that with increasing vertical loads, the impact forces change insignificantly, as also quantified by *PI* (Fig. 5-b). In contrast, displacement variations are notable, as u_{max} is reduced by 11.9%, 20.4% and 25.1% for SW, $SW+p_1$ and $SW+p_2$, respectively, with respect to the only-debris case (Fig. 5-c). These trends are likely due to vertical loads that increase the normal compressive stresses on bed mortar joints, which in turn increase the shear resistance [15]. The limited contribution of shear failure mechanisms to the structural capacity under out-of-plane debris impact loads [7] justifies the limited increase in *PI*.

Numerical F-t diagrams for load cases $SW+q_w$ are in Fig. 6-a for varying $\sigma_{t,m}$. No significant variations can be observed from the only-debris load case despite pre-impact damage (Fig. 6-b to f). The only notable variation is the lower initial loading rate for $\sigma_{t,m} = 0.07MPa$ (Fig. 6-a). This occurs because, despite the debris impacting the wall orthogonally (see Section 2.2), the pre-impact deformations caused by q_w lead to unparallel debris and wall surfaces. Indeed, it is known that a lower initial load rate is caused by unparallel debris-structure contact areas [20].

The *PI* variations are also minimal (Fig. 6-g). However, the unaltered diagrams observed when using q_w are unexpected. Indeed, pre-impact damage, reducing k_s, was expected to cause a further reduction in impact force. A possible explanation is the following. The impact force is governed by the structural resistance given by k_s and m_s, with inertia forces given by m_s governing the initial impact phase [22]. In the analyses, k_s decreases with structural damage, but m_s is unchanged, as well as the inertial contribution. Meanwhile, the subsequent impact phase is controlled by the debris damage, which is likely more important than the q_w damage. This aligns with the $PI - \mathrm{v}_d$ relationship also governed by inertia forces (see Section 3.1). The present data also show that q_w has a negative effect on displacements as u_{max} notably increases as q_w is included and $\sigma_{t,m}$ decreases (Fig. 6-h) due to the combined action of debris and q_w under decreasing $\sigma_{t,m}$.

3.4. High strain rate effects

The F-t diagrams obtained including the high strain rate effects in the material models, as explained in Section 2.1, are shown in Fig. 7-a. The load case only-debris is analysed here. It can be observed that considering DIF led to an insignificant increase of *PI* from 0.63 to 0.66 (+ 4.76%). Conversely, the effects on displacements are more significant, with u_{max} reduced by 16.9%, in line with [7]. These results indicate that high strain rate effects positively influence the impact scenario, which is expected considering the enhanced

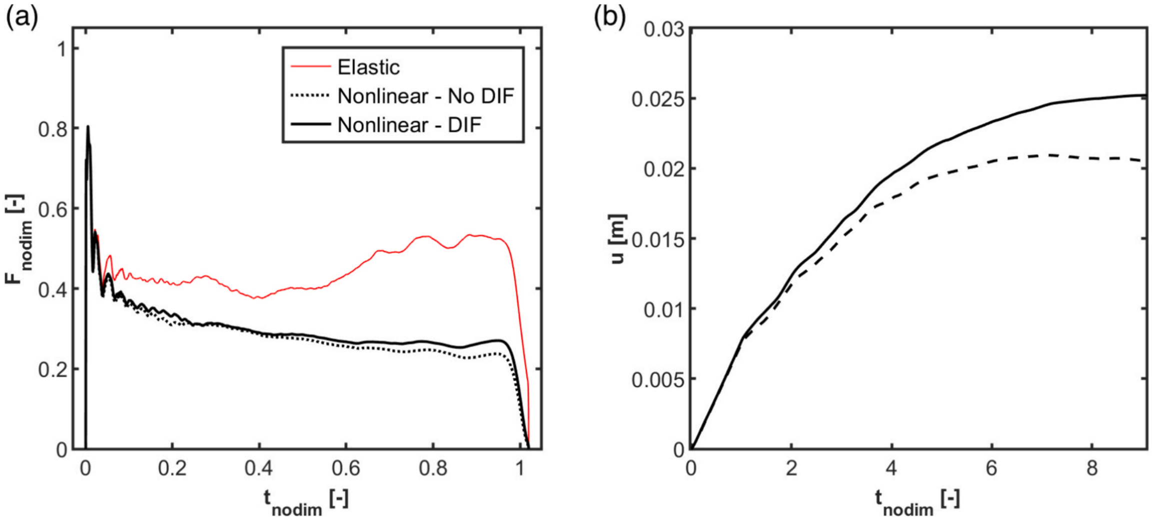

Fig. 7. (a) F-t diagrams and (b) u without and with DIF.

material performances given by the high strain rate effects (see Section 2.1).

4. Proposed analytical model

The Energy and Impulse-Momentum Model (EIMM) is proposed here to compute analytical nonlinear debris impact F-t diagrams. This model aims at replicating the numerical nonlinear F-t diagrams with a simplified curve. The EIMM F-t diagram is used in equivalent force impact models to simulate a reliable nonlinear structural response under debris impact loads. Therefore, the use of EIMM improves upon the higher computational and modelling efforts required for high-fidelity debris impact simulations on nonlinear structures, which are carried out with solid debris impact models. An overview of the EIMM conceptualisation is given in Fig. 8 in relation to the solid and equivalent impact models.

The data presented in Section 3 show that numerical nonlinear F-t diagrams have lower force values than the related numerical elastic F-t diagrams. Considering this, EIMM calculates the analytical nonlinear F-t diagram as a scaled version of the related analytical elastic F-t diagram. The scaling factor is determined by applying physically based compatibility equations to calculate the compatible F-t diagrams. These equations are based on the principle of energy conservation [30] and the impulse-momentum theorem [31]. In particular, the F-t diagram is correlated with the energy exchanged between debris and the structure, as well as with the change in momentum of the debris during the impact, as verified in Appendix C. Note that secondary impacts, i.e., impacts due to debris-structure interactions following the initial one, are not considered by the EIMM. This choice is based on [22], whose research, using comparable high-fidelity debris impact simulations, argued that debris may rotate in real events after the first contact due to debris-flow interactions. However, these interactions are not modelled in the present simulations, and such secondary impacts are likely unrealistic. The EIMM definition is presented in Section 4.1, the benchmark results are discussed in Section 4.2, while the model results are reported in Section 4.3. Critical results analyses and possible improvements are discussed in Section 4.4.

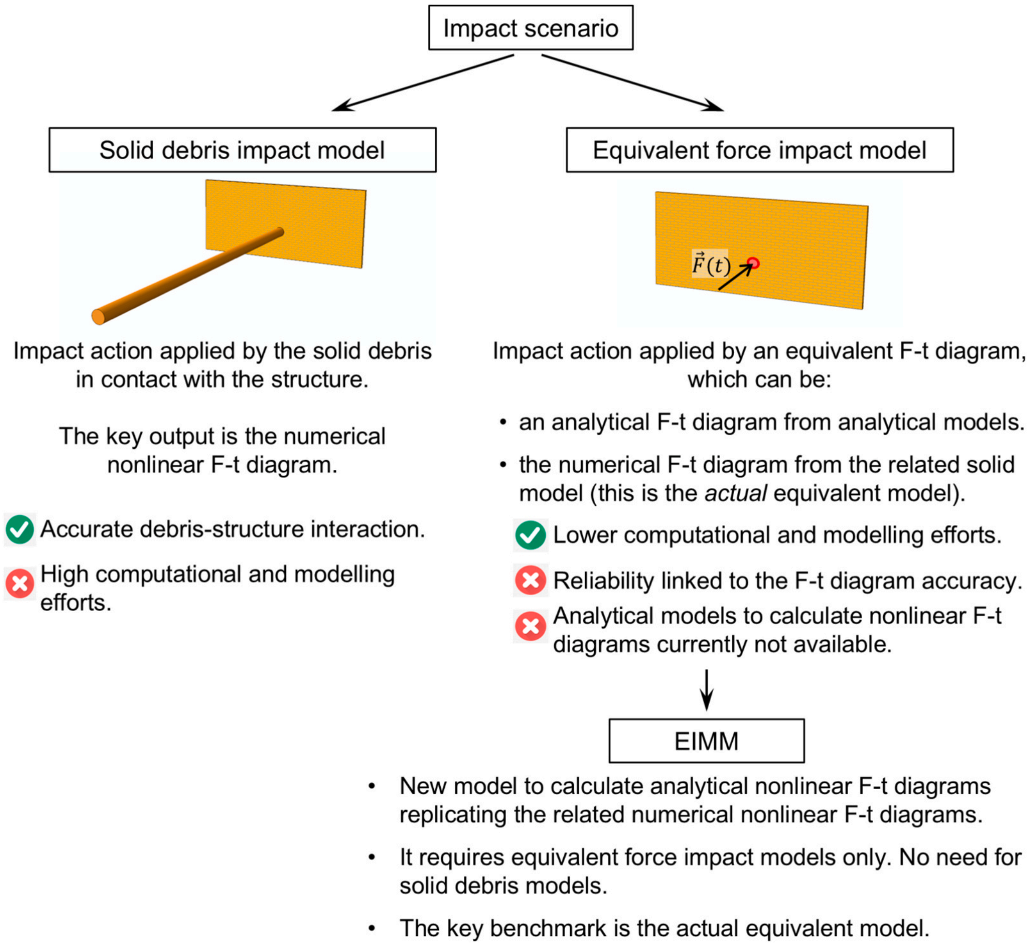

Impact action applied by the solid debris in contact with the structure.

The key output is the numerical nonlinear F-t diagram.

- ✓ Accurate debris-structure interaction.
- ✗ High computational and modelling efforts.

Impact action applied by an equivalent F-t diagram, which can be:

- an analytical F-t diagram from analytical models.
- the numerical F-t diagram from the related solid model (this is the *actual* equivalent model).

- ✓ Lower computational and modelling efforts.
- ✗ Reliability linked to the F-t diagram accuracy.
- ✗ Analytical models to calculate nonlinear F-t diagrams currently not available.

- New model to calculate analytical nonlinear F-t diagrams replicating the related numerical nonlinear F-t diagrams.
- It requires equivalent force impact models only. No need for solid debris models.
- The key benchmark is the actual equivalent model.

Fig. 8. Overview of the EIMM conceptualisation in relation to the solid and equivalent impact models.

4.1. Model definition

4.1.1. Application of the principle of energy conservation and impulse-momentum theorem

The energy balance principle states that the total energy of an isolated system is constant and that energy transforms as the system changes [30]. Energy conservation in numerical simulations is verified through an energy balance equation, such as [6]:

$$E_I + E_V + E_{FD} + E_K + E_{IHE} - E_W - E_{PW} - E_{CW} - E_{MW} - E_{HF} = E_{TOT} = constant \tag{8}$$

where E_I is the internal energy (e.g. strain energy), E_V is the viscous energy, E_{FD} is the frictional energy, E_K is the kinetic energy, E_{IHE} is the internal heat energy, E_W is the work done by external loads, E_{PW}, E_{CW} and E_{MW} are the work done by contact penalties, constraint penalties and added mass, respectively, and E_{HF} is the heat energy. The energy sum is the constant total energy E_{TOT}. The energy conservation principle is applied to the studied impact scenario as follows (Fig. 9). The initial condition is with the debris moving with uniform motion at velocity v_d (instant “0″). This condition changes only at the impact start (instant “1”), leading to $\mathrm{v}_{d,1} = \mathrm{v}_d$. Note that the energy first introduced into the system is the initial debris kinetic energy $E_{K,d,0}$, which is constant until the impact starts, leading to $E_{K,d,0} = E_{K,d,1}$. Energy transfer occurs after the impact starts, with part of $E_{K,d,1}$ becoming kinetic ($E_{K,s}$) and internal ($E_{I,s}$) structural energies, part becoming debris internal energy $E_{I,d}$ due to debris deformations, and another part dissipated as viscous (E_V) or friction (E_{FD}) energies. Thus, energies at the impact end (instant “2”) depend on the debris-structure interaction. The EIMM considers the energy variations between the impact initiation and end (Fig. 9).

For the EIMM purposes, Eq. (8) is simplified considering the energy components of high-fidelity simulations from Section 3. These components are weighed against the initial system energy, i.e. $E_{K,d,0}$ (Fig. 9). Fig. 10 shows that E_V, E_{PW} and E_{FD} are below 1.5% of $E_{K,d,0}$ between the impact start and impact end in various impact scenarios. The limited E_V is consistent with the absence of structural damping, with this contribution given only by default bulk viscosity introduced in the solution algorithm to prevent numerical instabilities under high-velocity loadings [6]. Moreover, E_{PW} is minimal as the default contact penalties in the numerical model effectively limit its value [6]. Also, perpendicular impacts limit sliding at the debris-structure interface, explaining the low E_{FD}. Consequently, E_V, E_{PW} and E_{FD} are neglected in formulating the EIMM.

Finally, E_{IHE} and E_{HF} are null as no heat transfer is involved, as well as E_{CW} and E_{MW} since constraint penalties and mass scaling are not implemented. Therefore, Eq. (8) becomes:

$$E_I + E_K - E_W = E_{TOT} \tag{9}$$

The energy balance equation (Eq. (9) is evaluated separately for the solid debris and equivalent force impact models. These equations are subsequently combined to form the compatibility equations, which are presented later in Section 4.1.2. For solid debris impact models, Eq. (9) is:

$$E_{K,d} + E_{I,d} + E_{K,s} + E_{I,s} - E_W^{add} = E_{TOT} \tag{10}$$

where E_W^{add} is the work done by the additional vertical and horizontal loads (see Section 2.2). Eq. (9) is initially evaluated at the beginning of simulation (instant “0″ in Fig. 9). Here, the structure is at rest position, $\mathrm{v}_{d,0} = \mathrm{v}_d$, and no loads are acting yet since loads are applied step-by-step starting from a null magnitude in FE simulations [6]. This leads to $E_{K,s,0} = E_{I,s,0} = E_{W,0}^{add} = 0$, while $E_{I,d,0}$ is also null as the debris is undeformed before the impact. Therefore, E_{TOT} is equal to $E_{K,d,0}$. Then, Eq. (9) is evaluated at the impact start and end, i.e. instants “1” and “2” in Fig. 9, respectively. Eq. (9) at the impact start and end is, respectively:

$$E_{K,d,1} + E_{I,d,1} + E_{K,s,1} + E_{I,s,1} - E_{W,1}^{add} = E_{TOT} \tag{11}$$

$$E_{K,d,2} + E_{I,d,2} + E_{K,s,2} + E_{I,s,2} - E_{W,2}^{add} = E_{TOT} \tag{12}$$

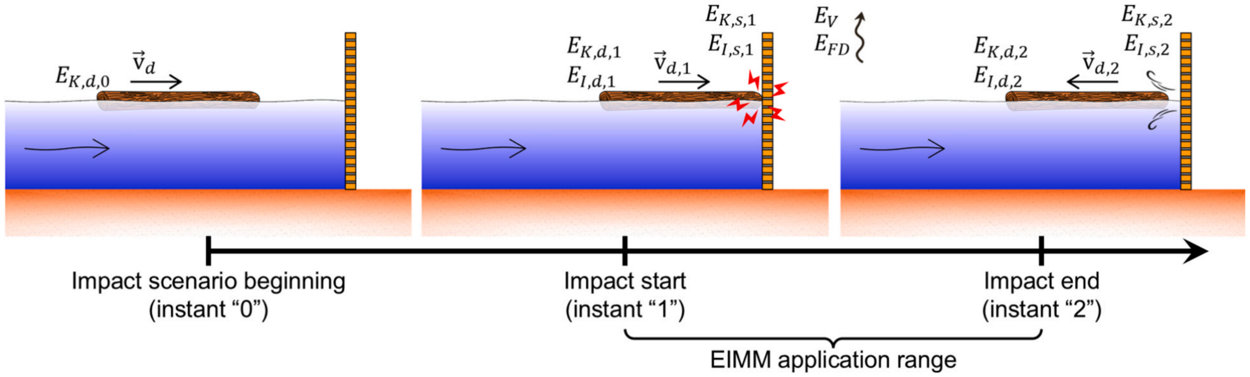

Fig. 9. Impact scenario timeline.

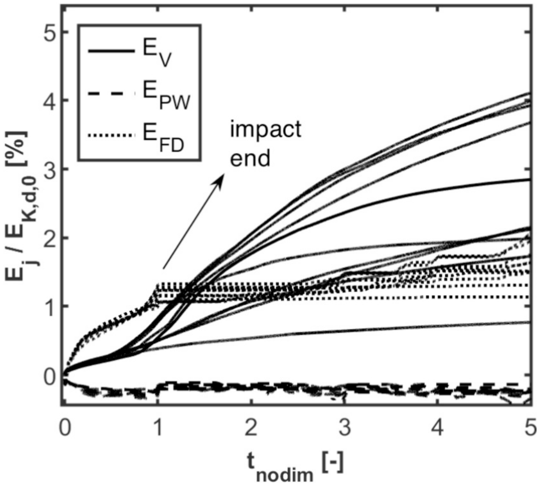

Fig. 10. E_V, E_{PW} and E_{FD} normalised with respect to $E_{K,d,0}$ in various impact scenarios.

here, $E_{I,d,1}$ is null as the debris is undeformed before the impact, while $E_{I,d,2}$ is neglected as the debris is unloaded and mostly undeformed after the impact, except for residual stress waves travelling along its body [20]. Note that $E_{K,s,1}$ and $E_{I,s,1}$ might not be zero because the application of other loads might precede the impact action, e.g. vertical and horizontal loads. Combining Eqs. (11) and (12), it follows that:

$$E_{K,d,1} + E_{K,s,1} + E_{I,s,1} - E_{W,1}^{add} = E_{K,d,2} + E_{K,s,2} + E_{I,s,2} - E_{W,2}^{add} \tag{13}$$

Thereafter, Eq. (9) is similarly evaluated for equivalent impact force models, for which Eq. (9) is:

$$\widetilde{E}_{K,s} + \widetilde{E}_{I,s} - \widetilde{E}_{W}^{add} - \widetilde{E}_{W}^{Ft} = \widetilde{E}_{TOT} \tag{14}$$

where the cap differentiates these energies from those of solid debris impact models and $\widetilde{E}_{W}^{Ft}$ is the work done by the applied F-t diagram. Again, at the beginning of the simulation, the structure is in its rest position, and no loads are acting yet. This leads to $\widetilde{E}_{K,s} = \widetilde{E}_{I,s} = \widetilde{E}_{W}^{add} = \widetilde{E}_{W}^{Ft} = 0$. Therefore, $\widetilde{E}_{TOT}$ is null. As for $E_{K,s,1}$ and $E_{I,s,1}$, also $\widetilde{E}_{K,s,1}$ and $\widetilde{E}_{I,s,1}$ might not be zero because the application of other loads might precede the impact action, e.g. vertical and horizontal loads. Now, the impact start and end are evaluated. Eq. (9) at the impact start and end is, respectively:

$$\widetilde{E}_{K,s,1} + \widetilde{E}_{I,s,1} - \widetilde{E}_{W,1}^{add} - \widetilde{E}_{W,1}^{Ft} = \widetilde{E}_{TOT} \tag{15}$$

$$\widetilde{E}_{K,s,2} + \widetilde{E}_{I,s,2} - \widetilde{E}_{W,2}^{add} - \widetilde{E}_{W,2}^{Ft} = \widetilde{E}_{TOT} \tag{16}$$

Combining Eqs. (15) and (16), it follows that:

$$\widetilde{E}_{K,s,1} + \widetilde{E}_{I,s,1} - \widetilde{E}_{W,1}^{add} = \widetilde{E}_{K,s,2} + \widetilde{E}_{I,s,2} - \widetilde{E}_{W,2}^{add} - \widetilde{E}_{W,2}^{Ft} \tag{17}$$

It is worth noting that all energy quantities can be directly obtained as output Abaqus variables. The only exception is the work of external loads, which cannot be saved for individual loads but only as a global variable, including the work done by all external loads in the simulation [6]. Therefore, E_{W}^{add} in solid debris impact models is directly obtained as the output Abaqus variable E_W since the vertical and horizontal actions are the only external loads. Instead, the F-t diagram is also working in equivalent force impact models, making $\widetilde{E}_W = \widetilde{E}_{W}^{add} + \widetilde{E}_{W}^{Ft}$. Thus, $\widetilde{E}_{W}^{Ft}$ is computed in post-processing analyses (see Appendix A), and $\widetilde{E}_{W}^{add}$ as:

$$\widetilde{E}_{W}^{add} = \widetilde{E}_W - \widetilde{E}_{W}^{Ft} \tag{18}$$

The impulse-momentum theorem states that the impulse I of a generic force applied to a body of mass m moving at velocity v is equal to the difference in the body momentum $\Delta(m\text{v})$ between the start and the end of the force application [31] as:

$$I = \Delta(m\text{v}) \tag{19}$$

It is clear that dissipative phenomena, such as friction and viscosity, are therefore neglected by this equation. Applying the impulse-momentum theorem (Eq. (19) between the impact start and end (instants “1″ and “2” in Fig. 9, respectively) leads to:

$$I = m_d(\mathrm{v}_{d,2} - \mathrm{v}_{d,1}) \tag{20}$$

Eqs. (13) and (20) are used to verify the assumed correlation between the impact F-t diagram and the energy exchanged between debris and the structure, as well as the change in debris momentum, respectively. These verifications are reported in Appendix C.

4.1.2. *Compatibility equations*

The compatibility equations are built by linking the energy balance equations of the solid debris (Eq. (13) and equivalent force (Eqs. (17) impact models. To do this, Eqs. (13) and (17) are rearranged as:

$$\begin{cases} E_{K,s,1} + E_{I,s,1} - E_{W,1}^{add} - E_{K,s,2} - E_{I,s,2} + E_{W,2}^{add} = -E_{K,d,1} + E_{K,d,2} & (a) \\ \widetilde{E}_{K,s,1} + \widetilde{E}_{I,s,1} - \widetilde{E}_{W,1}^{add} - \widetilde{E}_{K,s,2} - \widetilde{E}_{I,s,2} + \widetilde{E}_{W,2}^{add} = -\widetilde{E}_{W,2}^{Ft} & (b) \end{cases} \tag{21}$$

Then, their left- and right-hand sides are subtracted. Rearranging the terms, this leads to:

$$E_{K,d,1} - E_{K,d,2} - \widetilde{E}_{W,2}^{Ft} + \Delta E = 0 \tag{22}$$

where ΔE is the difference between the left-hand sides of Eq. 21-a and −b, computed as:

$$\Delta E = \left(E_{K,s,1} + E_{I,s,1} - E_{W,1}^{add} - E_{K,s,2} - E_{I,s,2} + E_{W,2}^{add}\right) - \left(\widetilde{E}_{K,s,1} + \widetilde{E}_{I,s,1} - \widetilde{E}_{W,1}^{add} - \widetilde{E}_{K,s,2} - \widetilde{E}_{I,s,2} + \widetilde{E}_{W,2}^{add}\right) \tag{23}$$

Furthermore, the properties of the actual equivalent model are exploited since the EIMM aims to replicate the results of such a model. It is then expected that the actual equivalent model results in comparable structural behaviour to that one modelled by the related solid debris impact model. It follows that:

$$E_{K,s,1} = \widetilde{E}_{K,s,1}, E_{I,s,1} = \widetilde{E}_{I,s,1}, E_{K,s,2} = \widetilde{E}_{K,s,2}, E_{I,s,2} = \widetilde{E}_{I,s,2}, E_{W,1}^{add} = \widetilde{E}_{W,1}^{add}, E_{W,2}^{add} = \widetilde{E}_{W,2}^{add} \tag{24}$$

The EIMM compatibility equations (Eqs. (25) are finally obtained by combining the principle of energy conservation and the impulse-momentum theorem. The former is considered in Eq. (25)-a, which is obtained by simplifying Eq. (22) assuming $\Delta E = 0$ in lieu of Eqs. (23) and (24). The latter is considered in Eq. (25)-b, which is obtained from Eq. (20). Moreover, the classical kinetic energy formula for $E_{K,d}$ is also considered to get Eqs. (25)-c, d. Thus, the compatibility equations are:

$$\begin{cases} E_{K,d,1} - E_{K,d,2} - \widetilde{E}_{W,2}^{Ft} = 0 & (a) \\ I = m_d(\mathrm{v}_{d,2} - \mathrm{v}_{d,1}) & (b) \\ E_{K,d,1} = \dfrac{1}{2} m_d \mathrm{v}_{d,1}^2 & (c) \\ E_{K,d,2} = \dfrac{1}{2} m_d \mathrm{v}_{d,2}^2 & (d) \end{cases} \tag{25}$$

It is worth noting that every term of the compatibility equations can be determined when using equivalent force impact models. The values of $\mathrm{v}_{d,1}$ and m_d are known quantities as these are initial conditions of the impact scenario, while I is calculated from the applied F-t diagram by using Eq. (6). The value of $\widetilde{E}_{W,2}^{Ft}$ is calculated as an output of the equivalent force impact model. $E_{K,d,1}$, $E_{K,d,2}$ and $\mathrm{v}_{d,2}$ are

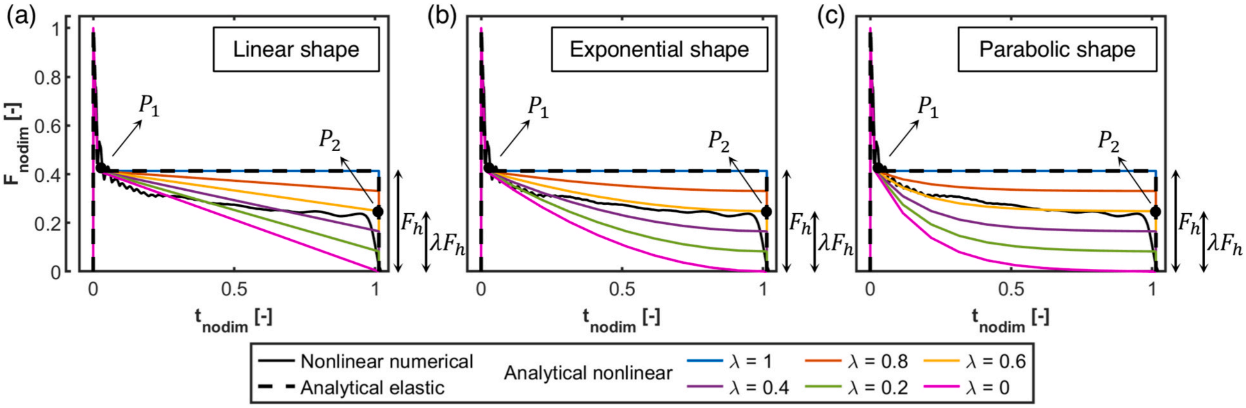

Fig. 11. Nonlinear analytical F-t diagrams with (a) linear, (b) exponential and (c) parabolic shapes.

calculated from Eqs. (25)-b,c,d once the aforementioned terms are determined. The procedure to use the compatibility equations is detailed in Section 4.1.3. It is also worth noting that assuming $\Delta E = 0$ is necessary to make the EIMM solvable with equivalent force impact models only. Indeed, ΔE depends on energy quantities also from solid debris impact models (see Eq. (24), which would be unknown in a procedure based solely on equivalent models such as the EIMM. This assumption is verified in Section 4.2 and the effects of its inaccuracies are discussed in Section 4.4.

4.1.3. Calculation of F-t diagrams

The calculation of the analytical nonlinear F-t diagrams with the EIMM is a step-by-step iterative procedure. The first step requires obtaining the elastic analytical F-t diagram, which serves as the starting diagram for computing the nonlinear one. Then, the yielding time t_y is calculated from the results of two preliminary impact simulations. Both of these simulations represent the impact load using the elastic analytical diagram, but one considers the elastic structure, while the other considers the nonlinear structure. The time t_y is identified as the time when the u time histories of the elastic and the nonlinear structure depart from each other. As such, t_y marks the limit after which the structural nonlinearities occur, and the elastic analytical F-t diagram loses its validity for $t > t_y$ because the nonlinear structural behaviour breaks the assumption of elastic structure used to calculate the elastic analytical diagram.

Therefore, the EIMM F-t diagram coincides with the elastic one for $t \leq t_y$. Instead, for $t > t_y$, the EIMM F-t diagram is a scaled version of the elastic one to mimic the relationship between nonlinear and elastic numerical F-t diagrams (see Fig. 3). The scaled portion of the analytical nonlinear F-t diagrams is defined between the points $P_1(t_1; F_1)$ and $P_2(t_2; F_2(\lambda))$, (Fig. 11). Here, $t_1 = t_y$ and F_1 equals the force of the elastic diagram at t_y. Instead, t_2 is the same as the total duration of the elastic impact, while $F_2(\lambda)$ equals the force of the elastic diagram F_h at t_2 scaled by a scaling factor λ (Fig. 11). The nonlinear diagram coincides with the elastic diagram if $\lambda = 1$, which is set as the upper bound for this parameter. A λ lower bound is not set, but if calculations lead to $\lambda < 0$, only the positive part of the analytical diagram is considered as the equivalent nonlinear diagram.

Moreover, the scaled diagram is designed to follow a specific shape function. Three shape functions, i.e. linear, exponential and parabolic, are defined in this paper (Fig. 11) and their results are compared to assess the most suitable one. Fig. 11 also reports the numerical nonlinear F-t diagram as a reference, along with the related analytical elastic F-t diagram (see Appendix E), to illustrate the scaling rationale. It is worth noting that Fig. 11 presents nondimensional F-t diagrams to align with the diagrams in Section 3, whereas EIMM calculations are performed using dimensional quantities. The equations of the shape functions are as follows. The equations for linear shapes are:

$$\begin{cases} F = a\,t + b \\ F(t_1) = F_1 \\ F(t_2) = F_2(\lambda) \end{cases} \tag{26}$$

The equations for exponential shapes are:

$$\begin{cases} F = a\,e^{c\ t} + b \\ F(t_1) = F_1 \\ F(t_2) = F_2(\lambda) \\ F'(t_1) = K(F_2(\lambda) - F_1)/(t_2 - t_1) \end{cases} \tag{27}$$

with the F' at t_1 considered as K times the slope of the line passing through P_1 and P_2. The value of K must be defined *a priori*. For this study, it is determined in Section 4.3.1 to get diagrams resembling the numerical nonlinear F-t diagrams presented in Section 3.1. The equations for parabolic shapes are:

$$\begin{cases} F = a\,t^2 + b\,t + c \\ F(t_1) = F_1 \\ F(t_2) = F_2(\lambda) \\ F'(t_2) = 0 \end{cases} \tag{28}$$

with the additional condition being that the vertex of the parabola is at P_2, which is chosen to mimic the numerical nonlinear F-t diagrams presented in Section 3. The parameters a, b and c that define these curves are calculated by solving the related systems of equations, i.e. Eqs. (26), 27 and 28, once P_1 and P_2 are set.

The correct scaling factor λ is determined through an iterative solution of the compatibility equations (Eqs. (25). The iterations are performed using the bisection method, a well-established generic iterative solution algorithm (see Appendix B). For this purpose, the compatibility equations are parametrised to λ as follows. First, Eq. (25)-a is rewritten as $H(\lambda)$:

$$H(\lambda) = E_{K,d,1} - E_{K,d,2}(\lambda) - \widetilde{E}^{Ft}_{W,2}(\lambda) = 0 \tag{29}$$

Here, $E_{K,d,1}$ is independent of λ and solely a function of the input m_d and $\mathrm{v}_{d,1} = \mathrm{v}_d$ (see Eq. (25)-c). Instead, $\widetilde{E}^{Ft}_{W,2}(\lambda)$ depends on λ as this is the work done by the λ-dependent analytical F-t diagram when used in the equivalent impact force model, i.e. the diagram controlled by the shape functions of Eqs. (26), 27 or 28. Moreover, $E_{K,d,2}(\lambda)$ depends on λ since it is computed with Eq. (25) c-d by using $\mathrm{v}_{d,2}(\lambda_i)$ calculated inverting Eq. (25)-b as:

$$\mathrm{v}_{d,2}(\lambda) = \frac{I(\lambda) + m_d \mathrm{v}_{d,1}}{m_d} \tag{30}$$

where $I(\lambda)$ is the impulse of the λ-dependent analytical F-t diagram.

The iterative steps are as follows. Initially calculate $E_{K,d,1}$ from the input m_d and $\mathrm{v}_{d,1} = \mathrm{v}_d$ with Eq. (25)-c. Then, for each iteration i the following is considered:

1. Set the value of λ_i and calculate the related λ-dependent analytical F-t diagram
2. Use this F-t diagram in an equivalent force impact model with the structure modelled as nonlinear. From these analyses, extract $\widetilde{E}^{Ft}_{W,2}(\lambda_i)$ and the maximum displacement $u_{max}(\lambda_i)$ caused by the λ_i-dependent F-t diagram.
3. Calculate $I(\lambda_i)$ with Eq. (6), then $\mathrm{v}_{d,2}(\lambda_i)$ with Eq. (30), then $E_{K,d,2}(\lambda_i)$ with Eq. (25)-d.
4. Evaluate $H(\lambda_i)$ with Eq. (29).
5. Calculate the relative errors γ_r for λ_i, $I(\lambda_i)$ and $u_{max}(\lambda_i)$ with Eq. B(3) and the error γ_H, calculated as:

   $$\gamma_H = \frac{H(\lambda)}{E_{K,d,0}} 100 \tag{31}$$

   which is a global metric for the residuals of Eq. (29) with respect to $E_{K,d,0}$, i.e. the energy initially put into the system (see Fig. 9).

6. Iterate steps 1–5 to refine λ_i using Eq. B(2) until γ_r and γ_H reach a minimum threshold. A ±5% error threshold is deemed acceptable in this study

Note that the bisection method requires an initial solution interval $[a_0, b_0]$ (see Appendix B). The value of a_0 is set to 1, which is the λ upper bound as discussed above. The value of b_0 is suggested equal to 0, which is associated with a diagram having P_2 on the horizontal axis (Fig. 11). The F-t diagrams shown in Section 3 convey that $b_0 = 0$ is low enough to represent the typical scenarios, but every initial interval must be checked using Eq. B(1). If not verified, b_0 must be reduced until Eq. B(1) is satisfied. It is worth noting that the true errors γ_T (Eq. B(4) are also computed for I and u_{max} to verify the accuracy of the EIMM results. The used true data are those of the actual

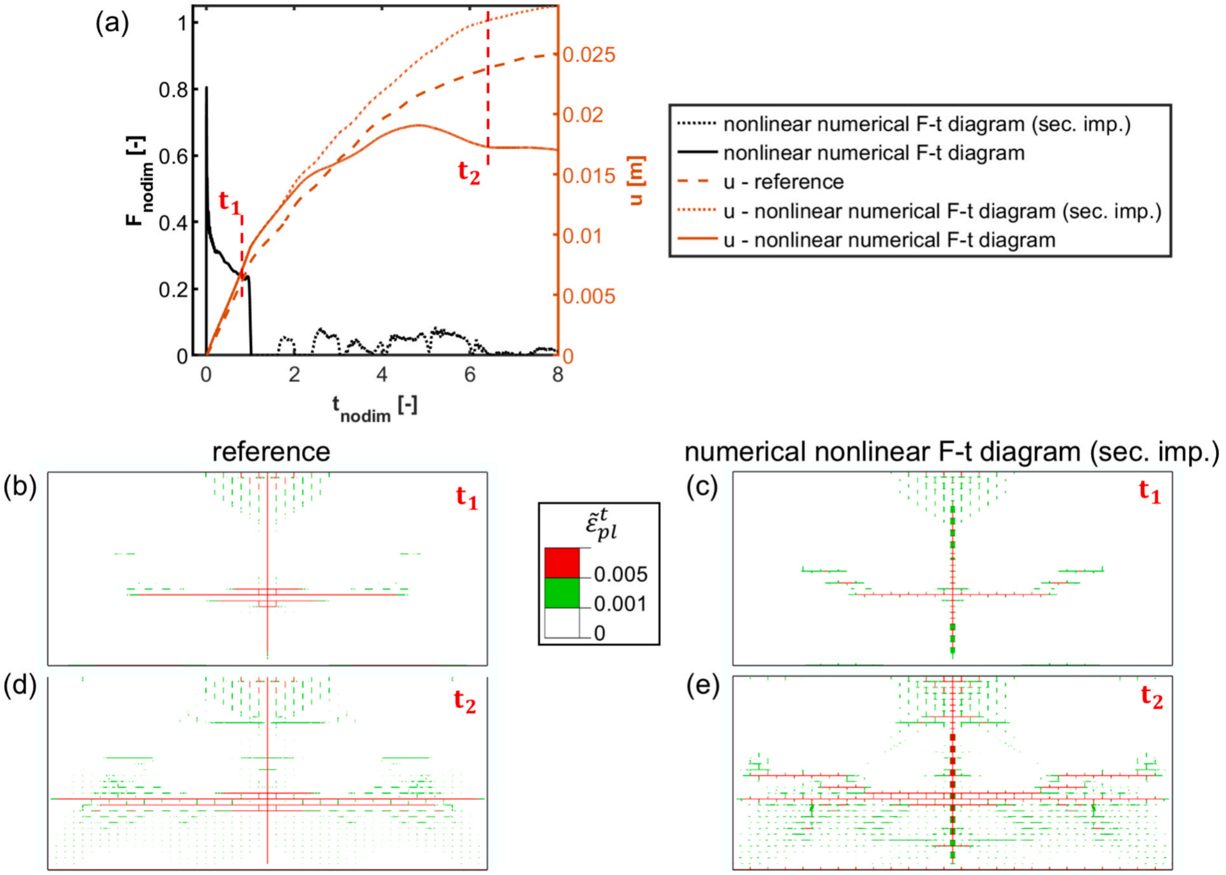

Fig. 12. Comparison between reference and actual equivalent impact force models in terms of (a) u and damage patterns at (b, c) t_1 and (d, e) t_2.

equivalent force impact model, which is the selected benchmark for EIMM (see introduction to Section 4).

4.2. Discussion of the benchmark accuracy

The benchmark used to assess the EIMM results is the actual equivalent force model. This benchmark is appropriate because the EIMM aims to replicate the numerical nonlinear F-t diagrams with simplified curves, which is the diagram applied in the actual equivalent model (Fig. 8). As such, EIMM results are expected to match those of the actual equivalent model. At the same time, the actual equivalent force model is expected to match the results of the related solid debris impact model as the actual model considers the F-t diagram measured from the solid model, i.e. the numerical nonlinear F-t diagram. Therefore, the accuracy of the actual equivalent model is preliminarily verified in terms of u, damage patterns and energies. The load cases only-debris, $SW+p$ and $SW+q_w$ are analysed, taking the results of Section 3 as a reference. This verification is quantified with the errors:

$$\gamma_{actual,u}=\frac{\widetilde{u}_{max}-u_{max}}{u_{max}}100,\qquad \gamma_{actual,E}=\frac{\widetilde{E}-E}{E}100,\qquad \gamma_{actual,E,tot}=\frac{\widetilde{E}-E}{E_{K,d,0}}100,\qquad \gamma_{actual,E,glob}=\frac{\Delta E}{E_{K,d,0}}100 \tag{32}$$

The error $\gamma_{actual,u}$ evaluates $\widetilde{u}_{max}$ of the actual equivalent model against u_{max} of the related solid impact model. The error $\gamma_{actual,E}$ evaluates the difference between the equivalent force model energies $\widetilde{E}$ relatively to those of the solid debris model E, while $\gamma_{actual,E,tot}$ evaluates the absolute energy variations $\widetilde{E}-E$ in relation to the energy of the initial system $E_{k,d,0}$ (Fig. 9). Finally, the error $\gamma_{actual,E,glob}$ quantifies the mathematical weight of assuming $\Delta E = 0$ in formulating Eq. (25)-a.

The u time-history for the actual equivalent force impact model and the related solid debris impact model in the load case only-debris are compared in Fig. 12. Secondary impacts, excluded from the EIMM formulation (see introduction to Section 4), must be

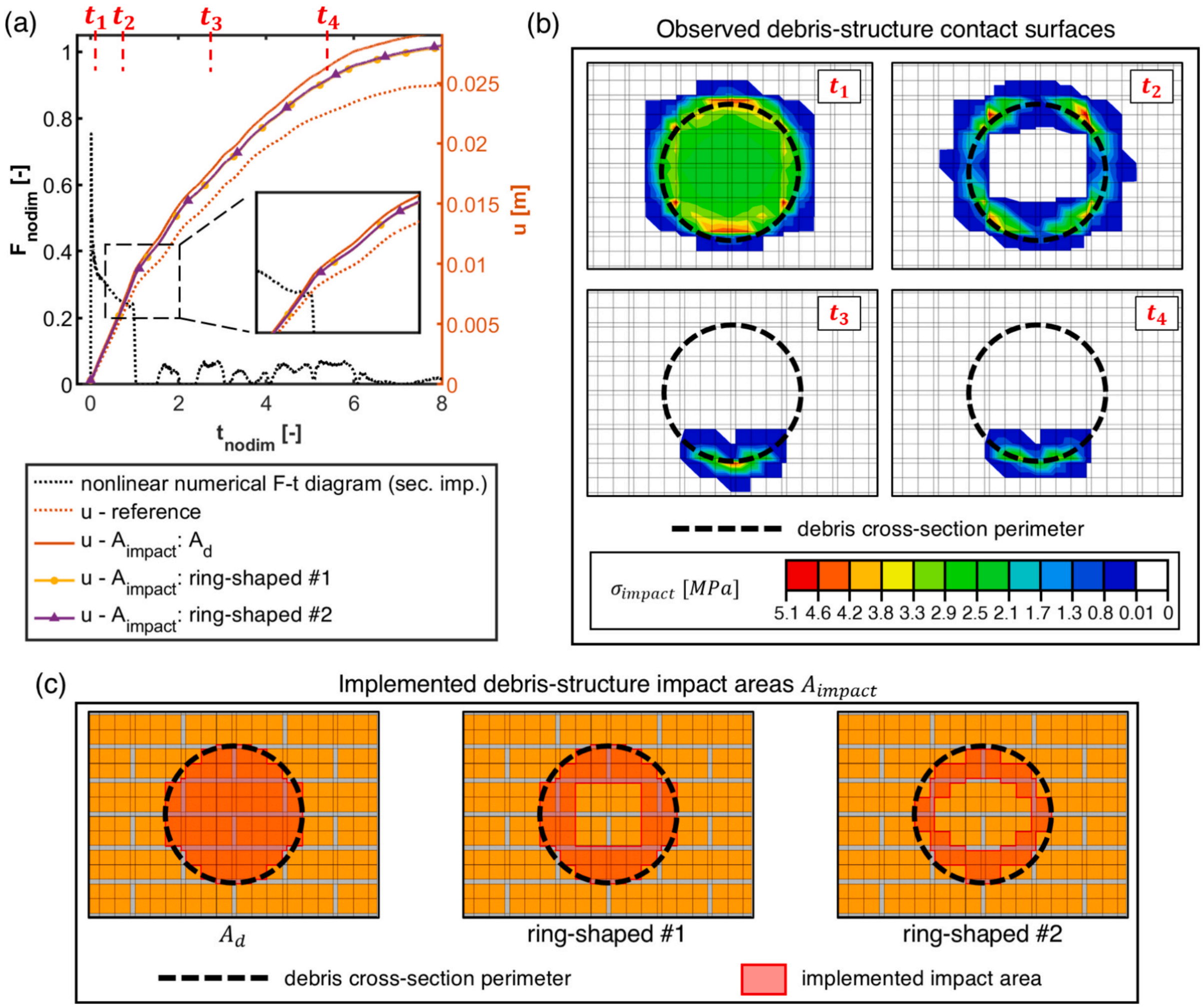

Fig. 13. (a) Displacement time histories, (b) observed debris-structure contact surfaces, and (c) implemented debris-structure impact areas.

included in these analyses for consistency. This is required to apply an F-t diagram in the equivalent model that is the same exact force experienced by the structure in the related solid model (see the label “sec. imp.” in Fig. 12).

Results show that displacements are overestimated by the actual equivalent model (Fig. 12-a), with $\gamma_{actual,u} = 19.1\%$. Damage is also overestimated, but crack patterns are well predicted by the actual equivalent model (Fig. 12-b to g). Since secondary impacts are not considered by the EIMM, the actual model excluding secondary impacts is also calculated. These results show that displacements expectedly coincide until secondary impacts arise and u_{max} decreases by 55% (Fig. 12-a). Similar trends and errors occur for the load cases $SW+p$ and $SW+q_w$. The energy errors $\gamma_{actual,E}$, $\gamma_{actual,E,tot}$ and $\gamma_{actual,E,glob}$ (Eqs. (32) are computed in different load cases for the energy components of Eqs. (24). In load case only-debris, $\widetilde{E}_{K,s,1}$, $\widetilde{E}_{I,s,1}$ and $\widetilde{E}_{W}^{add}$ are null as no additional loads are present, leaving the structure unloaded before the impact. Thus, all errors are null for these quantities. Instead, positive $\gamma_{actual,E}$ are observed for $\widetilde{E}_{K,s,2}$ and $\widetilde{E}_{I,s,2}$, conveying that actual equivalent model overestimates structural energies. Comparable errors occur in load cases $SW+p_1$ and $SW+q_w$. However, all load cases have acceptable values of $\gamma_{actual,E,tot}$ and $\gamma_{actual,E,glob}$ ranging between -5% and 17%, which convey a limited mathematical weight of assuming $\Delta E = 0$ in formulating Eq. (25)-a. Detailed error values are reported in Appendix C.

The cause behind these errors is discussed hereafter. The actual equivalent model has the F-t diagram directly recorded from high-fidelity simulations. Therefore, the observed errors cannot be caused by inaccuracies in the F-t diagram and must be identified elsewhere. As such, deeper analyses are done on the results of the reference high-fidelity simulations. Here, data show that the debris-structure contact area and stresses σ_{impact} are space- and time-dependent (Fig. 13-a, b). As expected, the contact area is initially

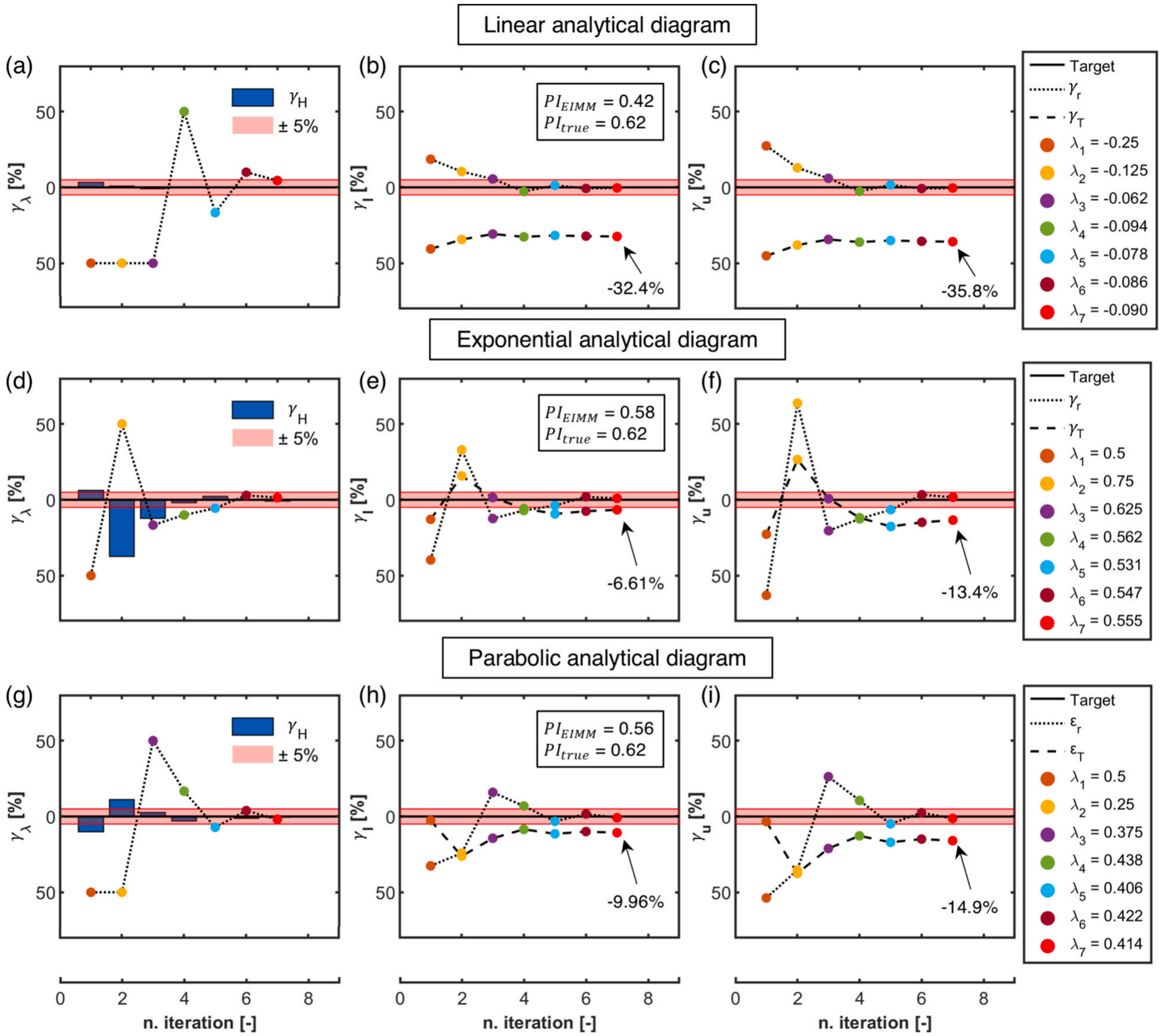

Fig. 14. Results of the EIMM using (a,b,c) a linear analytical diagram type, (d,e,f) an exponential analytical diagram type and (g,h,i) a parabolic analytical diagram type.

comparable to the debris cross-section A_d, with a mostly uniform σ_{impact} distribution ($t = t_1$). Successively, this area transforms to a ring-shape with nonuniform σ_{impact} distribution ($t = t_2$). This is likely due to bodies deformations, which break the initial debris-structure surface parallelism. The impact area further reduces to edge-contacts and causes σ_{impact} concentrations ($t \geq t_3$) likely due to the further increasing structural deformations.

Therefore, the observed debris-structure contact area and stresses (Fig. 13-b) are different from the impact area defined in the equivalent impact force models, where the F-t diagram is applied as uniform pressure over A_{impact} equal to A_d (see Section 2.2). This difference is likely the cause of the errors observed for the actual equivalent model. This possibility is verified by modifying A_{impact} in the actual equivalent impact model. Two alternative ring-shaped areas are defined to mimic the observed contact surfaces (Fig. 13-c). The impact force is still implemented as a uniform pressure over A_{impact} to observe the influence of a single changing parameter. The structural displacements u obtained when using the ring-shaped areas are reported in Fig. 13-a, which are associated with $\gamma_{actual,u} \cong$ 12% for both the ring-shaped areas. Note that this error improved from the case using $A_{impact} = A_d$. Similarly, the ring-shaped areas also improve the energy errors $\gamma_{actual,E}$, $\gamma_{actual,E,tot}$ and $\gamma_{actual,E,glob}$ (see Appendix C). Yet, some inaccuracies remain, which are likely due to the missed implementation of the final edge-contact area and the varying stress distribution (Fig. 13-c). These adjustments are outside the scope of this study, and their investigation is postponed to future research, as also discussed in Section 4.4.

In conclusion, the results presented in this section show that the actual equivalent impact model overestimates the reference high-fidelity simulation results given by the solid debris impact model. Moreover, data show that this overestimation is likely caused by how the impact force is implemented in the equivalent model in terms of A_{impact} and pressure distribution over it. Nonetheless, the actual model is still representative of the solid debris impact model in terms of u, crack patterns and energies. Therefore, the actual equivalent model is a suitable benchmark for the EIMM in the absence of further improvements to its accuracy, which is postponed to future research. Note that the results excluding secondary impacts are considered as benchmark since these impacts are not implemented in the EIMM.

It is finally worth noting that the presented results suggest that the EIMM underpredicts the results of the actual equivalent model. This is due to the positive $\gamma_{actual,E,glob}$, which means positive ΔE (see Eqs. (32). As such, in Eq. (25)-a, $E_{K,d,1}$ is constant and lower values of $E_{K,d,2}$ and $\widetilde{E}^{Ft}_{W,2}$ are required to satisfy such an equation if a positive ΔE is neglected. A lower $\widetilde{E}^{Ft}_{W,2}$ is associated to a F-t diagram with lower magnitude, since the work done by a force is directly proportional to its magnitude. Consequently, the impulse I is also reduced, leading to reducing $v_{d,2}$ (Eq. (30) and $E_{K,d,2}$ (Eq. (25)-d). This expected underestimating EIMM is discussed in Sections 4.3 and 4.4.

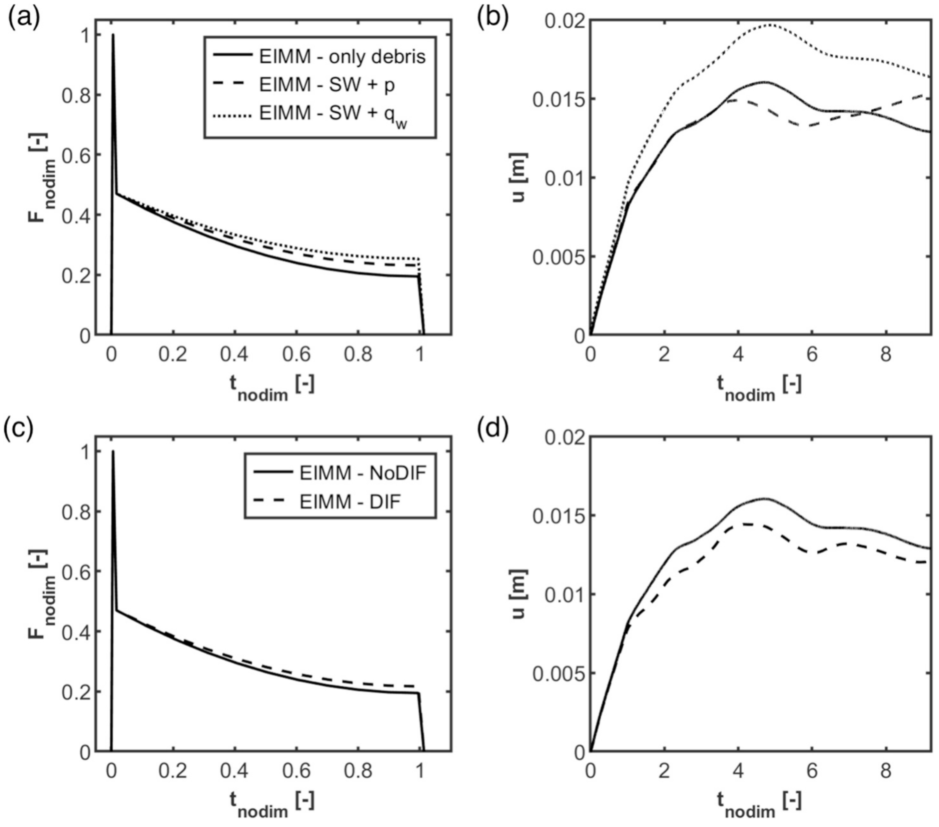

Fig. 15. Results of the EIMM in load cases $SW + p$ and $SW + q_w$: (a) F-t diagrams and (b) u. Results of the EIMM in including DIF in material models: (c) F-t diagrams and (d) u.

4.3. Model results

4.3.1. Only-debris load case

The EIMM is applied in this section to the only-debris load case (Fig. 14). Three different shape functions are tested for the analytical diagrams, i.e. linear, exponential and parabolic shapes (Fig. 11), and their results are compared. Note that the parameter K needed by the exponential diagrams is set equal to 5 to ensure resemblance with the numerical diagrams of Section 3.1. The initial solution interval $[a_0, b_0]$ is set to $[0, 1]$ for the exponential and parabolic diagrams, while it is set to $[-0.5, 0]$ for the linear diagrams. The baseline v_d and $\sigma_{t,m}$ are used. The acceptable error threshold of ±5% is passed by γ_H in 1, 4 and 3 iterations for the linear, exponential and parabolic diagrams, respectively (Fig. 14-a,d,g). Conversely, the relative errors γ_r for λ, I and u converge slower, and require around 6 iterations to pass such a threshold (Fig. 14).

These data show that the EIMM requires limited iterations to converge to a solution independently from the shape of the analytical diagram. However, different F-t diagram shapes significantly influence the true errors γ_T. Linear diagrams result in significant γ_T for I (-32.2%) and u (-61.5%) (Fig. 14-b,c). Exponential and parabolic shapes result in better γ_T, being -6.61% for I and -13.4% for u (Fig. 14-e,f), and -9.96% for I and -14.9% for u (Fig. 14-h,i), respectively. The values of γ_T for PI are the same as for I.

Note that the negative γ_T indicates that the EIMM underestimates the impact force, which is expected (see Section 4.4). However, γ_T are significantly higher when using linear shapes. This is likely due to the notable differences between linear shapes and the numerical nonlinear diagrams (Fig. 11-a). As such, linear shapes are not recommended. In contrast, exponential and parabolic shapes result in similar and limited γ_T. Nonetheless, the exponential equations (Eq. (27) are difficult to generalise due to the required *a priori* definition of K. Without sufficient data to generalise K, the parabolic shape is recommended and adopted next.

4.3.2. Including additional loads and high strain rate effects

The EIMM applied for load cases $SW + q$ and $SW + q_w$ converges with similar speeds and results in comparable γ_T as the only-debris load case (Section 4.3.1), i.e. $\cong 6 - 10\%$. Moreover, as in high-fidelity simulations (Section 3.3), the EIMM also calculates F-t diagram and displacement variations with respect to the only-debris load case (Fig. 15). In load case $SW + p$, the F-t diagram increase, which

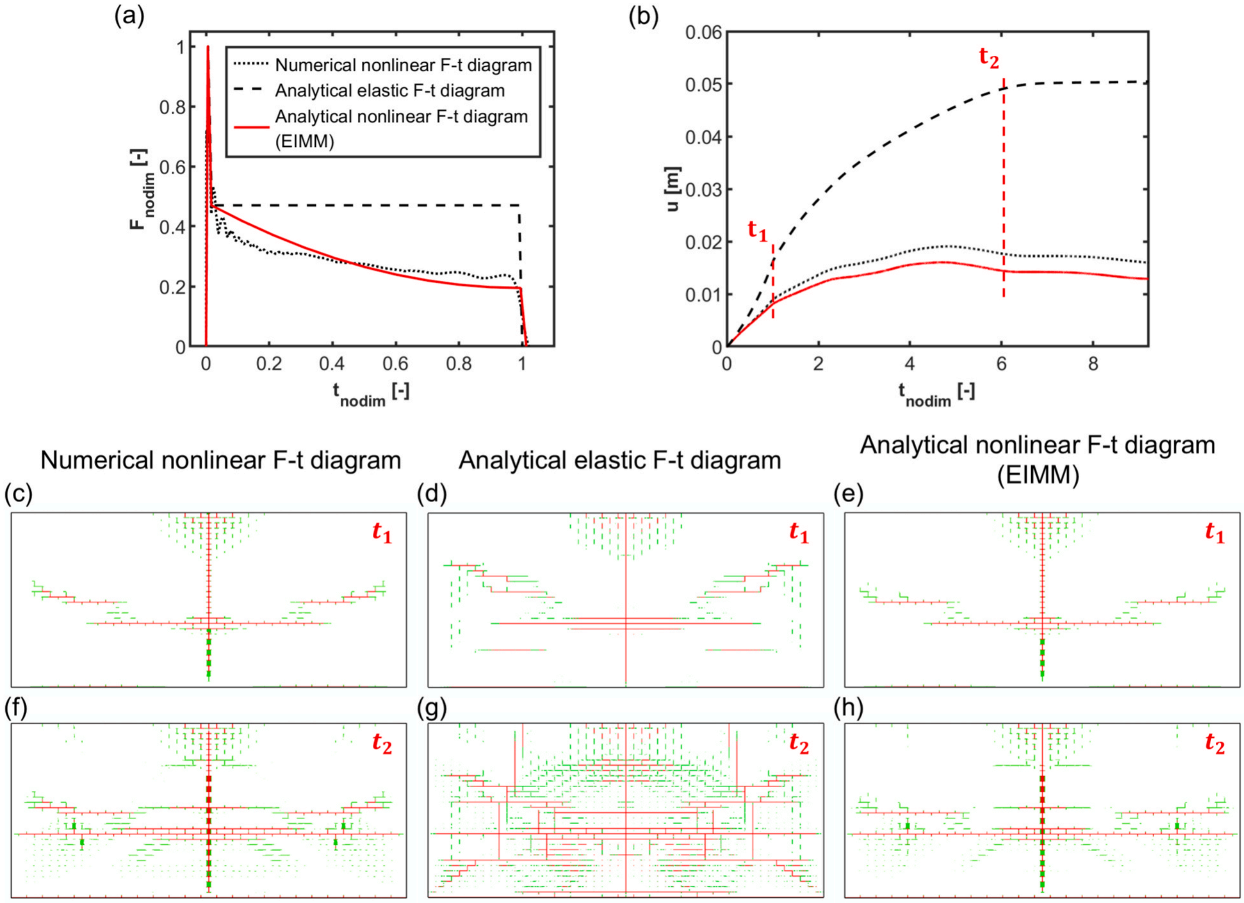

Fig. 16. Comparing numerical, analytical elastic and analytical nonlinear (EIMM) models in terms of (a) F-t diagrams, (b) u and damage patterns at (c, d, e) t_1 and (f, g, h) t_2.

aligns with Fig. 5-a. Instead, u initially decreases as expected, but eventually increases (Fig. 15-a), marking a difference with Fig. 5-b. Moreover, in load case $SW + q_w$, the F-t diagram and displacements increase. The latter aligns with Fig. 6-h, but the former is not observed in Fig. 6-a. These results show that the EIMM mostly adapts to different load cases. The observed differences with high-fidelity simulations are likely due to different dynamic behaviours induced in equivalent force impact models, whose investigation is postponed to future research. The detailed data of the EIMM application for load cases $SW + q$ and $SW + q_w$ are reported in Appendix D.

The EIMM applied for the only-debris load case with included high strain rate effects in the material models, i.e. using DIF, converges with similar speeds and results in comparable γ_T as the only-debris load case without DIF, i.e. $\cong 6 - 10\%$ (see Section 4.3.1). Moreover, the EIMM results in variations of F-t diagrams and structural displacements in line with those observed in high-fidelity simulations, i.e. higher impact force (with PI increasing by 3.9%) and lower u_{max} (-10.6%) (see Fig. 15). This demonstrates that the EIMM adapts to the modified structural behaviour function of the strain rate dependent materials response. The detailed data of the EIMM application for load cases that include DIF are reported in Appendix D.

4.4. Critical results analysis and possible improvements – Case-study analysis

The EIMM results are critically analysed in a representative case study that has the baseline structure and debris properties in the only-debris load case. This case-study is simulated using three different equivalent force impact models, each representing the debris action with a numerical nonlinear F-t diagram, an analytical elastic F-t diagram and an analytical nonlinear F-t diagram. The numerical nonlinear F-t diagram is the one calculated in Section 3.2 using high-fidelity simulations. The results of this simulation are used as a reference. The analytical elastic F-t diagram is the one previously presented in Fig. 11. This option represents the current state-of-the-art for debris impact analyses, where the F-t diagrams are calculated using elastic analytical models, despite potential structural nonlinearities (see Section 1). Finally, the nonlinear analytical F-t diagram is the one previously calculated using the proposed EIMM in Section 4.3.1.

The results show that the analytical elastic F-t diagram significantly overestimates both impact force (Fig. 16-a), with I being 62.6% higher, and displacements (Fig. 16-b), with u_{max} being 164.6% higher. Note that these errors are due to the structural nonlinear behaviour and not to model errors (see Appendix E. Crack patterns, presented at $t_1 = 1$ and $t_2 = 6$ (Fig. 16-b), are also notably more severe under the analytical elastic diagram (Fig. 16-d,g). Moreover, applying Eq. (29) to the results of this simulation results to $\gamma_H = -109\%$, demonstrating that the analytical elastic diagram is incompatible with the impact scenario. These results point out the inaccuracy of assuming elastic structures in computing the analytical F-t diagrams if structural nonlinearities occur. In contrast, the analytical nonlinear F-t diagram computed with the EIMM is more accurate (Fig. 16-a), with the error for I and PI improves to -9.96%. The error for u_{max} improves to -14.9% (Fig. 16-b). Finally, crack patterns are well predicted (Fig. 16-e,h). Note that, while the EIMM displacement errors are unsafe, PI errors are safe. Indeed, a lower PI indicates a worse performance of the structure under the considered impact load (see Section 3). The safe calculation of PI is a significant advantage of the EIMM because it allows for a performance-based design procedure with conservative results. For example, given a minimum design PI threshold, the EIMM would lead to a conservative structural design to meet this threshold. Instead, the unconservative displacement calculations discourage the use of the EIMM for a displacement-based design procedure. Nonetheless, displacement errors are limited, and their values remain representative of the global structural behaviour, as also conveyed by the well-predicted crack patterns.

Given these results, the EIMM improves upon the significantly overestimated results obtained by using elastic analytical F-t diagrams for nonlinear structures, which is the current state-of-the-art (see Section 1). Moreover, these data show that EIMM is a valid new numerical strategy to reliably analyse debris impacts on nonlinear structures. Here, given a specific debris impact demand, real practice applications can be carried out to assess the structural performance of existing structures under such debris, or to design a new structure that satisfies minimum performance thresholds.

Finally, errors γ_T ranging between -10% and -15% are commented to identify possible improvements for the EIMM. These errors are likely due to the assumed $\Delta E = 0$ in defining Eq. (25)-a, while its value is $\cong 10 - 17\%$ of $E_{K,d,1}$ (see $\gamma_{actual,E,glob}$ in Appendix C). To verify this error source, the EIMM is reapplied by adding a fictitious constant term equal to $0.1 E_{K,d,1}$ in Eq. (25)-a to compensate for the neglected ΔE. The only-debris and $SW + q_w$ load cases are analysed as representative examples. This fictitious term lead to more accurate results, with γ_T around $1 - 2\%$ (see Appendix D), confirming the causation between the EIMM accuracy and the neglected ΔE. Moreover, ΔE depends on how the F-t diagram is implemented in terms of A_{impact} and pressure distribution (see Section 4.2). It follows that the EIMM errors likely depends on the same reasons. Therefore, while the fictitious term added above cannot be generalised, future EIMM improvements must work on more accurate implementations of the F-t diagrams. These studies would also generally improve the accuracy of equivalent force impact models.

5. Conclusions

This study investigated the effects of structural failure on debris impact F-t diagrams and proposed a new model, the Energy and Impulse Momentum Model (EIMM), to calculate analytical nonlinear F-t diagrams. High-fidelity Finite Element simulations were used to collect the reference data for different impact scenarios of log debris impacts on masonry walls. Moreover, the proposed EIMM consisted of a simplified iterative procedure based on physically-based compatibility equations formulated from the energy conservation principle and the impulse-momentum theorem.

The main findings can be summarised as follows:

- Structural failure resulted in a reduction of the impact force that was proportional to the damage experienced by the structure during the impact.
- This reduction was quantified with the Performance Indicator (*PI*), which was calculated as the ratio between the impulses of the nonlinear and elastic F-t diagrams. *PI* was calculated in a range between 0.8 and 0.4 for the common scenarios investigated. This parameter was proposed as a potential design parameter in performance-based design methods.
- The proposed EIMM could effectively compute nonlinear analytical F-t diagrams, also generically integrating the effects of different external loads and material properties.
- Results showed that the EIMM improved upon the highly overestimated results of applying analytical elastic diagrams to nonlinear structures, which is the current practice. True errors γ_T from using the EIMM were around 10–15 % for *PI* and structural displacements, against the 63 % and 165 %, respectively, calculated from using the current practice. Moreover, the results conveyed advantageous real practice applications in performance-based design procedures as the EIMM calculated safe *PI* values.

Limitations of the EIMM remain in how the impact force is implemented in terms of the impact area and pressure distribution. Critical error analyses showed that correcting such aspects would lead to more accurate EIMM outputs. These corrections would also generally improve the accuracy of equivalent force impact models and will be investigated in future studies. Further extensions of the presented research will also include debris nonlinearities to simulate more comprehensive nonlinear debris-structure interactions.

CRediT authorship contribution statement

Alessandro De Iasio: Writing – review & editing, Writing – original draft, Visualization, Validation, Software, Resources, Methodology, Investigation, Formal analysis, Data curation, Conceptualization. **Riccardo Briganti:** Writing – review & editing, Writing – original draft, Supervision, Project administration, Methodology, Formal analysis, Conceptualization. **Gabriele Milani:** Writing – review & editing, Methodology, Conceptualization. **Bahman Ghiassi:** Writing – review & editing, Writing – original draft, Supervision, Project administration, Funding acquisition, Formal analysis, Conceptualization.

Declaration of competing interest

The authors declare that they have no known competing financial interests or personal relationships that could have appeared to influence the work reported in this paper. The author Gabriele Milani is an editor of this journal. In accordance with policy, Gabriele Milani was blinded to the entire peer review process.

Acknowledgements

The Faculty of Engineering of the University of Nottingham (UK) is acknowledged for funding Alessandro De Iasio's PhD scholarship. The University of Nottingham HPC cluster Ada has been accessed to perform the numerical simulations. B. Ghiassi gratefully acknowledges the Department ABC of Politecnico di Milano, which provided financial support for his visiting professorship at Politecnico di Milano within project NEST 2025 https://www.dabc.polimi.it/en/research/nest-project/.

Appendix A

The post-processing calculation of the impact force work in equivalent impact force models ($\widetilde{E}^{Ft}_{W,2}$) is carried out by applying the classical definition of work, i.e. the product of the acting force times the caused displacement. This definition is exploited as follows. The F-t diagram is applied as a uniform pressure on A_{impact} with total force $F(t)$ (see Section 2.2). This area covers a number of mesh nodes equal to *nnodes*, each of them indexed with j ranging from 1 to *nnodes*. The force acting on the j-th node is $F_j(t) = F(t)/nnodes$. The horizontal displacement of the j-th node u_j is calculated, while vertical displacements are neglected as the impact force is horizontal. Despite the pressure load is a follower load, i.e. it remains perpendicular to the elements faces during the analysis [6], the vertical components of F_j are also neglected, approximating the horizontal components equal to F_j assuming that their inclinations with respect to the horizontal direction are small. Therefore, the instantaneous work done by the F_j is equal to $F_j du_j/dt$, and $\widetilde{E}^{Ft}_{W,2}$ is computed as:

$$\widetilde{E}^{Ft}_{W,2} = \int_0^{t_d} \sum_{j=1}^{nnodes} F_j(t) \frac{du_j(t)}{dt} dt \tag{A1}$$

To solve this equation using the simulations output, Eq. A(1) is simplified as follows. The force $F_j(t)$ is the same for every node and can be taken out of the summation over the surface nodes to get:

$$\widetilde{E}^{Ft}_{W,2} = \int_0^{t_d} F_j(t) \sum_{j=1}^{nnodes} \frac{du_j(t)}{dt} dt \tag{A2}$$

Then, expressing $du_j(t)/dt$ in discretised form as $\Delta u_j(t)/\Delta t$, it follows that:

$$\sum_{j=1}^{nnodes}\frac{\Delta u_j(t)}{\Delta t} = \frac{1}{\Delta t}\sum_{j=1}^{nnodes}\Delta u_j(t) = \frac{1}{\Delta t}\left[u_{1,2}(t) - u_{1,1}(t) + u_{2,2}(t) - u_{2,1}(t) + \ldots + u_{j,2}(t) - u_{j,1}(t)\right] \tag{A3}$$

Collecting the terms, with u_{TOT} being the summation of the nodal displacements, we get:

$$u_{TOT,2}(t) = u_{1,2}(t) + u_{2,2}(t) + \ldots + u_{j,2}(t)$$

$$u_{TOT,1}(t) = u_{1,1}(t) + u_{2,1}(t) + \ldots + u_{j,1}(t) \tag{A4}$$

$$\sum_{j=1}^{nnodes}\Delta u_j(t) = \Delta u_{TOT}(t) \tag{A5}$$

It results that:

$$\widetilde{E}_{W,2}^{Ft} = \int_0^{t_d} F_j(t)\frac{\Delta u_{TOT}(t)}{\Delta t}dt \tag{A6}$$

which is solved with the trapezoidal rule using the simulation time-steps. The validity of these post-processing calculations is assessed as follows. An equivalent impact force model is defined in the only-debris load case such that the F-t diagram is the sole external force. This allows the use of the Abaqus output variable $\widetilde{E}_W$ as a benchmark since only the F-t diagram contributes to it. The baseline properties of Section 3.1 and the actual F-t diagram are used. The relative error γ_{Ew} is computed for $\widetilde{E}_W^{Ft}$ computed with Eq. A(6) against the Abaqus output variable $\widetilde{E}_W$. Fig. A1 shows that the post-processing calculation of $\widetilde{E}_W^{Ft}$ underestimate the Abaqus output variable results, but $\gamma_{Ew} = 1.34\%$ at maximum, validating such calculations.

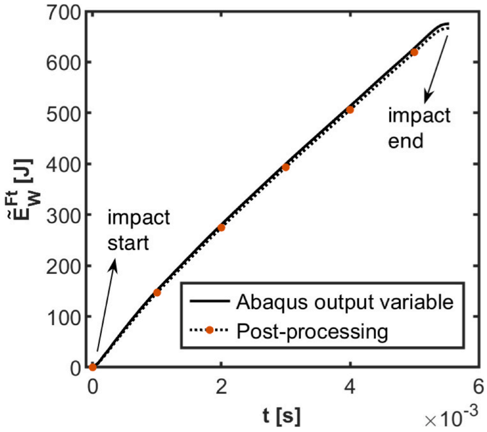

Fig. A1. $\widetilde{E}_W^{Ft}$ from the related Abaqus output variable and proposed post-processing calculations.

Appendix B

The bisection method belongs to the family of numerical methods to solve analytical equations whose solution cannot be expressed in closed form [32], such as the equation $H(\lambda)$ of the EIMM model (i.e. Eq. (29). These methods are based on successive solution refining through an iterative procedure starting from an initial guessed value. The convergence of the approximated solution λ_i to the true solution λ_T with an increasing number of iterations i is required for such methods to be effective. The rate at which λ_i converge to λ_T is the rate of convergence. Among the available strategies, the bisection method is used.

The choice of the bisection method is motivated hereafter. This method is often avoided because it exhibits first-order convergence, resulting in a relatively high number of iterations required to achieve an acceptable solution [32,33]. As such, 2nd other convergence methods are commonly preferred, like the Newton-Raphson or secant methods. Nonetheless, the bisection method has less strict requirements for solution convergence than other methods. Given an initial guessed interval $[a_0, b_0]$ that contains the solution of the function $H(\lambda)$ to solve, the requirements of the bisection method are the continuity of $H(\lambda)$ in the interval $[a_0, b_0]$ and:

$$H(a_0)H(b_0) < 0 \tag{B1}$$

Conversely, the Newton-Raphson and secant methods also require that $H(\lambda)$ is monotonous in the interval $[a_0, b_0]$. However, this condition is not guaranteed for the equation to be solved in this study. This is demonstrated by applying a series of scaled F-t diagrams with parabolic F-t diagram shapes and λ ranging from 0 to 1. Two different structures are analysed using $\sigma_{t,m} = 0.58MPa$ and $\sigma_{t,m} =$

$0.15 MPa$, which are taken from the values of $\sigma_{t,m}$ considered analysing structural nonlinearities. The function $H(\lambda)$ is not monotonic in the first case (Fig. B1-a), while it is monotonic in the second case (Fig. B1-b). Therefore, the monotonicity of $H(\lambda)$ cannot be generalised for the problems analysed in this study, and numerical methods that require such a condition, e.g. the Newton-Raphson method, are not recommended.

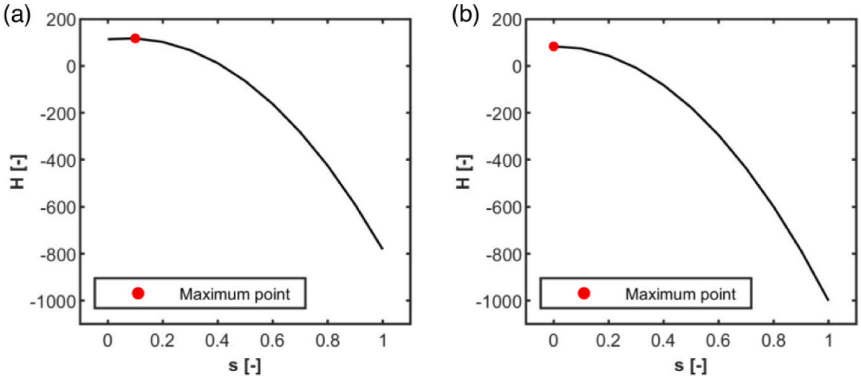

Fig. B1. $H(\lambda)$ using parabolic analytical F-t diagrams and $\sigma_{t,m}$ equal to (a) 0.58 MPa and (b) 0.15 MPa.

The bisection method is applied as follows. The values of a_0 and b_0 are initially defined such that Eq. B(1) is satisfied. The first approximated solution is $\lambda_1 = (a_0 + b_0)/2$. Then, the solution interval is refined to $[a_0, \lambda_1]$ or $[\lambda_1, b_0]$ by adapting Eq. B(1). In general, the i^{th} approximated solution is:

$$\lambda_i = \frac{a+b}{2}, \text{ with } \begin{cases} a = a_{i-1}, \ b = \lambda_{i-1}, & \text{if } F(a_{i-1}) \cdot F(\lambda_{i-1}) < 0, \\ a = \lambda_{i-1}, \ b = b_{i-1}, & \text{if } F(\lambda_{i-1}) \cdot F(b_{i-1}) < 0 \end{cases} \quad i = 1, 2, 3, \ldots \tag{B2}$$

The iterative procedure is monitored with the relative error $\gamma_{r,i}$, computed as:

$$\gamma_{r,i} = \frac{\Omega_i - \Omega_{i-1}}{\Omega_{i-1}} \tag{B3}$$

where Ω_i is a generic parameter to indicate λ_i or any other simulation output, e.g. $u_{max,i}$, selected based on the analysis needs. Iterations are stopped when $\gamma_{r,i}$ is lower than a suitable arbitrary threshold. The true error $\gamma_{T,i}$ can also be evaluated as:

$$\gamma_{T,i} = \frac{\Omega_i - \Omega_T}{\Omega_T} \tag{B4}$$

Obviously, Ω_T needs to be known to compute $\gamma_{T,i}$, which is not the case when solving unknown problems, but it is in assessing the accuracy of iterative methods in problems with known solutions, such as in this study.

Appendix C

The correlation between the impact F-t diagrams and the energy conservation and impulse-momentum theorem equations, Eqs. (13) and (20), respectively, is verified using the errors γ_1 and γ_2. These errors are computed as the relative difference of the left-hand side against the right-hand side of Eqs. (13) and (20), respectively. The values of $v_{d,1}$ and $v_{d,2}$ in Eq. (20) are computed from $E_{K,d,1}$ and $E_{K,d,2}$, respectively, using the classic definition of kinetic energy, i.e. $E_K = 0.5mv^2$. The data from the high-fidelity simulations of Section 3 are used as a reference. The errors γ_1 and γ_2 are reported in Table C1. These errors are negative, which is expected given the neglected energies in Eq. (13) and the neglected dissipative phenomena like friction and viscosity in Eq. (20) (see Section 4.1.1).

Table C1
Values of γ_1 and γ_2 related to applying Eqs. (13) and (20) in reference simulations.

Case	γ_1	γ_2	Case	γ_1	γ_2
only debris – $\sigma_{t,m} = 1.16\,MPa$	−2.27 %	−1.77 %	SW	−4.52 %	−3.05 %
only debris – $\sigma_{t,m} = 0.58\,MPa$	−2.81 %	−1.46 %	$SW + p_1$	−4.34 %	−2.95 %
only debris – $\sigma_{t,m} = 0.29\,MPa$	−3.63 %	−1.27 %	$SW + p_2$	−4.19 %	−2.71 %
only debris – $\sigma_{t,m} = 0.15\,MPa$	−4.31 %	−1.18 %	$q_w - \sigma_{t,m} = 1.16\,MPa$	−4.12 %	−2.51 %
only debris – $\sigma_{t,m} = 0.07\,MPa$	−4.72 %	−1.15 %	$q_w - \sigma_{t,m} = 0.58\,MPa$	−4.58 %	−2.41 %
only debris – $v_d = 0.50\,m/s$	−1.35 %	−2.23 %	$q_w - \sigma_{t,m} = 0.29\,MPa$	−5.82 %	−1.29 %
only debris – $v_d = 1.78\,m/s$	−3.31 %	−1.63 %	$q_w - \sigma_{t,m} = 0.15\,MPa$	−6.69 %	−1.47 %
only debris – $v_d = 3.00\,m/s$	−4.12 %	−1.18 %	$q_w - \sigma_{t,m} = 0.07\,MPa$	−6.11 %	−0.66 %
only debris – $v_d = 4.00\,m/s$	−4.62 %	−1.22 %	DIF	−3.11 %	−2.96 %

(continued on next page)

Table C1 (*continued*)

Case	γ_1	γ_2	Case	γ_1	γ_2
only debris – $v_d = 5.00\,m/s$	−4.80 %	−1.29 %	–	–	–
only debris – $v_d = 6.00\,m/s$	−4.84 %	−1.43 %	–	–	–

It is worth noting the increasing trend of γ_1 for decreasing $\sigma_{t,m}$ or increasing v_d, i.e. for increasing structural damage. This is due to the neglected $E_{I,d,2}$ in Eq. (13) (Section 4.1.1). Indeed, higher amounts of $E_{I,d,2}$ are retained by the debris due to the lower capacity of more damaged structures to absorb the impact energy, as conveyed by the ratio $E_{I,d,2}/E_{TOT}$ in Fig. C1-a,b. This leads to unbalance Eq. (13), but $E_{I,d,2}/E_{TOT}$ is limited for various impact scenarios. Moreover, the average γ_1 and γ_2 are limited and equal to −4.47% and −1.84%, with standard deviations being 1.14% and 0.73%, respectively, allowing to verify Eqs. (13) and (20).

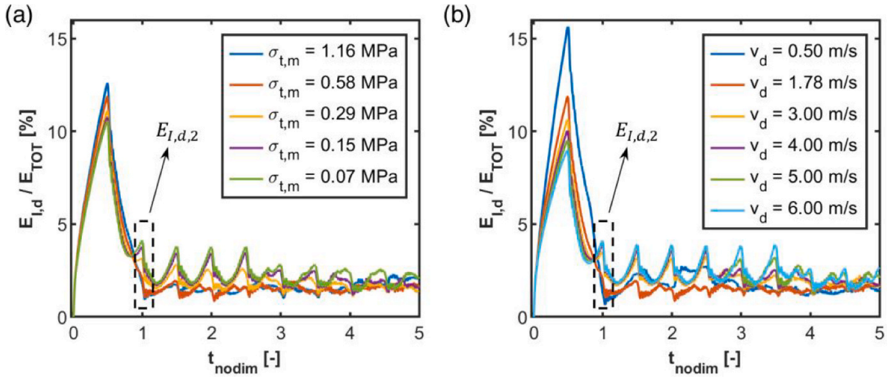

Fig. C1. Ratio $E_{I,d}/E_{TOT}$ for varying (a) $\sigma_{t,m}$ and (b) v_d.

Furthermore, Table C2 reports the energy errors $\gamma_{actual,E}$, $\gamma_{actual,E,tot}$ and $\gamma_{actual,E,glob}$ (Eqs. (32) calculated in different load cases. Note that in load case only-debris, $E_{K,s,1}$, $E_{I,s,1}$, $\widetilde{E}_{K,s,1}$, $\widetilde{E}_{I,s,1}$, E_W^{add} and $\widetilde{E}_W^{add}$ are null as no additional loads are present, leaving the structure unloaded before the impact. Also, note that $\gamma_{actual,E}$ for $\widetilde{E}_{W,2}^{add}$ is significant likely due to calculation errors in $\widetilde{E}_{W,2}^{Ft}$ (see Appendix A), that consequently affect Eq. (18). Instead, Table C3 reports the same errors when varying the impact area.

Table C2
Errors $\gamma_{actual,E}$, $\gamma_{actual,E,tot}$ and $\gamma_{actual,E,glob}$ for different load cases.

	only-debris			$SW + p_1$			$SW + q_w$		
[%]	$\gamma_{actual,E}$	$\gamma_{actual,E,tot}$	$\gamma_{actual,E,glob}$	$\gamma_{actual,E}$	$\gamma_{actual,E,tot}$	$\gamma_{actual,E,glob}$	$\gamma_{actual,E}$	$\gamma_{actual,E,tot}$	$\gamma_{actual,E,glob}$
$E_{K,s,1}$	0	0	16.01	0	0	11.88	0	0	16.91
$E_{I,s,1}$	0	0		0	0		0	0	
$E_{K,s,2}$	22.99	8.69		25.02	9.05		28.84	10.49	
$E_{I,s,2}$	18.49	7.31		16.28	6.29		15.67	6.42	
$E_{W,1}^{add}$	0	0		0	0		0	0	
$E_{W,2}^{add}$	0	0		94.49	−3.09		−1886.5	−4.54	

Table C3
Errors $\gamma_{actual,E}$, $\gamma_{actual,E,tot}$ and $\gamma_{actual,E,glob}$ for different A_{impact} (load case: $SW + q_w$).

	A_{impact}– full cross-section			A_{impact}– ring-shaped #1			A_{impact}– ring-shaped #2		
[%]	$\gamma_{actual,E}$	$\gamma_{actual,E,tot}$	$\gamma_{actual,E,glob}$	$\gamma_{actual,E}$	$\gamma_{actual,E,tot}$	$\gamma_{actual,E,glob}$	$\gamma_{actual,E}$	$\gamma_{actual,E,tot}$	$\gamma_{actual,E,glob}$
$E_{K,s,1}$	0	0	16.91	0	0	12.92	0	0	13.01
$E_{I,s,1}$	0	0		0	0		0	0	
$E_{K,s,2}$	28.84	10.49		24.30	10.49		24.79	9.02	
$E_{I,s,2}$	15.67	6.42		9.97	6.42		10.82	4.43	
$E_{W,1}^{add}$	0	0		0	0		0	0	
$E_{W,2}^{add}$	−1886.5	−4.54		−1840.3	−4.1		−1852.6	−4.32	

Appendix D

The EIMM detailed results in load cases $SW + p$ and $SW + q_w$ are shown in Fig. D1. The EIMM detailed results in load case only-debris and including DIF in material models are shown in Fig. D2. The EIMM detailed results adding the fictitious energy correction term are shown in Fig. D3.

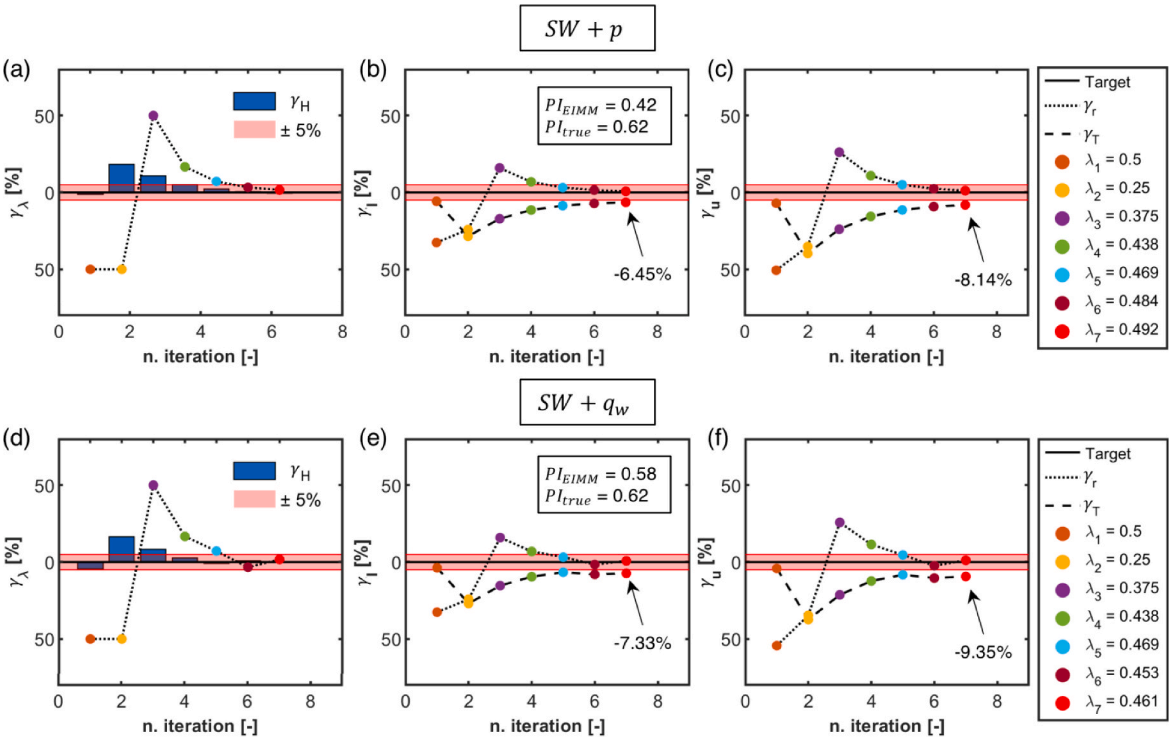

Fig. D1. EIMM applied in load cases (a,b,c) $SW + p$ and (d,e,f) $SW + q_w$.

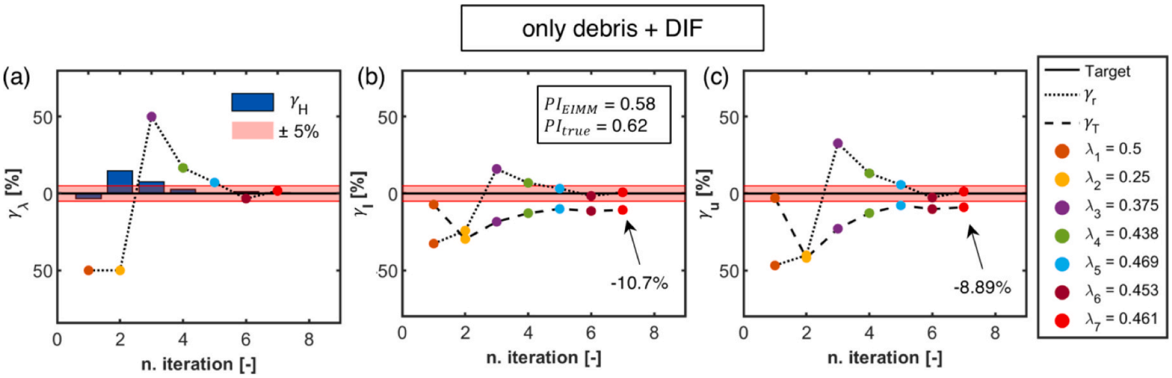

Fig. D2. EIMM applied in load case only-debris and including DIF in material models.

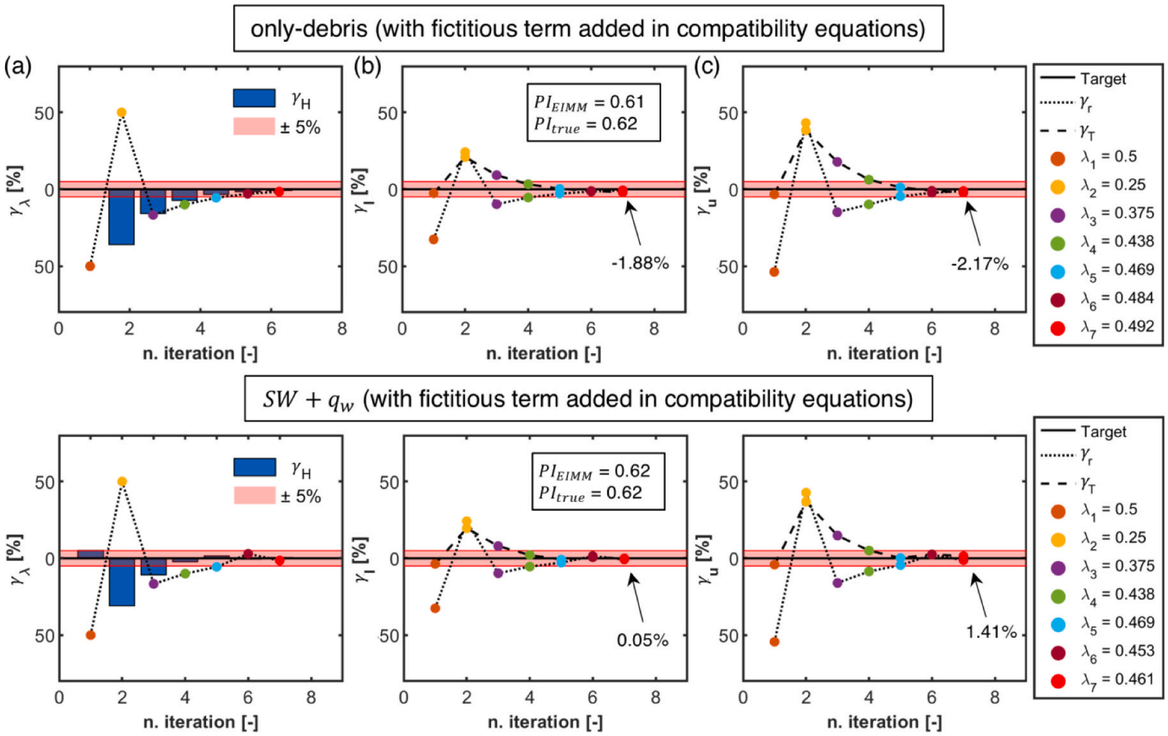

Fig. D3. Modified EIMM in load cases (a,b,c) only-debris and (d,e,f) $SW + q_w$.

Appendix E

The elastic analytical F-t diagram of the impact scenario defined in Section 2.2 is calculated following [22]. The selected scenario is associated with structure-to-debris mass (μ) and stiffness (δ) ratios equal to 5.29 and 0.25, respectively, which are associated with the Mass and Stiffness Ratios Model (MSRM) to compute analytical elastic F-t diagrams. This elastic diagram is shown in Fig. E1-a. Moreover, the inaccuracies of the analytical elastic F-t diagram discussed in relation to Fig. 16 are due to the nonlinear structural behaviour and not to model errors. This is demonstrated by analysing the same scenario but with the structure modelled as fully elastic. Indeed, F-t diagrams (Fig. E1-a) and u are well predicted (Fig. E1-b) in the case of elastic structural behaviour, with errors being 3.01% for I and 5.04% for u_{max}, in line with existing literature [22].

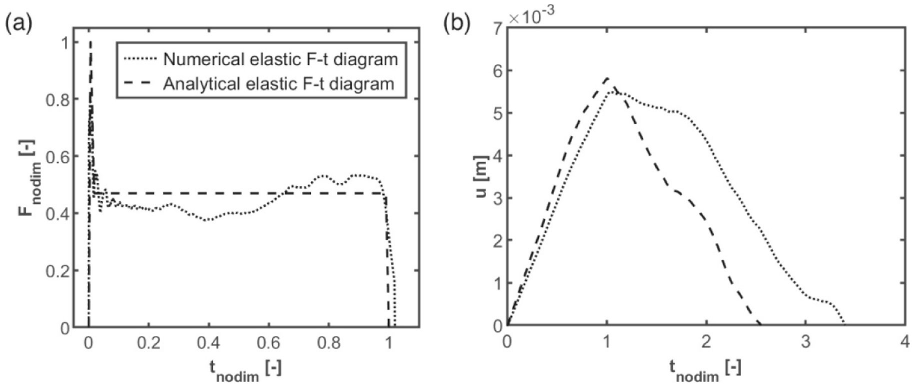

Fig. E1. (a) F-t diagrams and (b) structural displacements for elastic numerical and analytical models.

Data availability

Data will be made available on request.

References

[1] C. Naito, M. Asce, C. Cercone, S.M. Asce, H.R. Riggs, D. Cox, Procedure for site assessment of the potential for tsunami debris impact, J. Waterw. Port Coast Ocean Eng. 140 (2014) 223–232, https://doi.org/10.1061/(ASCE)WW.1943-5460.0000222.
[2] ASCE, Minimum Design Loads and Associated Criteria for Buildings and Other Structures (ASCE/SEI 7-22), Reston, VA, 2022.
[3] F. Jalayer, S. Carozza, R. De Risi, G. Manfredi, E. Mbuya, Performance-based flood safety-checking for non-engineered masonry structures, Eng. Struct. 106 (2016) 109–123, https://doi.org/10.1016/j.engstruct.2015.10.007.
[4] D. Wüthrich, P.A. Korswagen, H. Selvam, J. Oetjen, J. Bricker, H. Schüttrumpf, Field survey assessment of flood loads and related building damage from the July 2021 event in the Ahr Valley (Germany), J. Flood Risk Manage. (2024), https://doi.org/10.1111/JFR3.13024.
[5] P. Piran Aghl, C.J. Naito, H.R. Riggs, Estimation of demands resulting from inelastic axial impact of steel debris, Eng. Struct. 82 (2015) 11–21, https://doi.org/10.1016/j.engstruct.2014.10.021.
[6] Abaqus, Abaqus User Manual, Dassault Systèmes Simulia Corp, United States, 2018.
[7] A. De Iasio, B. Ghiassi, R. Briganti, G. Milani, High strain rate effects in masonry structures under waterborne debris impacts, Eng. Struct. 297 (2023) 116911, https://doi.org/10.1016/J.ENGSTRUCT.2023.116911.
[8] V.L. Chong, The behaviour of laterally loaded masonry panels with openings, University of Plymouth, 1993.
[9] P.B. Lourenço, An anisotropic macro-model for masonry plates and shells: implementation and validation, 1997.
[10] B. Pantò, F. Cannizzaro, I. Caliò, P.B. Lourenço, Numerical and experimental validation of a 3D Macro-model for the in-plane and out-of-plane behavior of unreinforced masonry walls, Int. J. Archit. Heritage 11 (2017) 946–964, https://doi.org/10.1080/15583058.2017.1325539.
[11] B. Ghiassi, G. Milani, Numerical modelling of masonry and historical structures: From theory to application, Numerical Modeling of Masonry and Historical Structures: From Theory to Application (2019) 1–795. https://doi.org/10.1016/C2017-0-01579-3.
[12] A. Drougkas, P. Roca, C. Molins, Numerical prediction of the behavior, strength and elasticity of masonry in compression, Eng. Struct. 90 (2015) 15–28, https://doi.org/10.1016/j.engstruct.2015.02.011.
[13] B. Alfarah, F. López-Almansa, S. Oller, New methodology for calculating damage variables evolution in plastic damage model for RC structures, Eng. Struct. 132 (2017) 70–86, https://doi.org/10.1016/j.engstruct.2016.11.022.
[14] D.A. Hordijk, Local approach to fracture of concrete, Delft University of Technology, 1991.
[15] R. Pluijm, Out-of-plane bending of masonry: behaviour and strength, Technische Universiteit Eindhoven, 1999. https://doi.org/10.6100/IR528212.
[16] H. Hao, B.G. Tarasov, Experimental study of dynamic material properties of clay brick and mortar at different strain rates, in: Australian Journal of Structural Engineering, Engineers Media, 2008: pp. 117–132. https://doi.org/10.1080/13287982.2008.11464992.
[17] I. Nistor, N. Goseberg, J. Stolle, Tsunami-driven debris motion and loads: a critical review, Front. Built Environ. 3 (2017), https://doi.org/10.3389/fbuil.2017.00002.
[18] G. Ruffini, R. Briganti, P. De Girolamo, J. Stolle, B. Ghiassi, M. Castellino, Numerical modelling of flow-debris interaction during extreme hydrodynamic events with DualSPHysics-CHRONO, Appl. Sci. 11 (2021) 3618, https://doi.org/10.3390/APP11083618.
[19] G. Ruffini, J.M. Domínguez, R. Briganti, C. Altomare, J. Stolle, A.J.C. Crespo, B. Ghiassi, S. Capasso, P. De Girolamo, MESH-IN: a MESHed INlet offline coupling method for 3-D extreme hydrodynamic events in DualSPHysics, Ocean Eng. 268 (2023) 113400, https://doi.org/10.1016/j.oceaneng.2022.113400.
[20] K. Paczkowski, H.R. Riggs, C.J. Naito, A. Lehmann, A one-dimensional model for impact forces resulting from high mass, low velocity debris, Struct. Eng. Mech. 42 (2012) 831–847, https://doi.org/10.12989/SEM.2012.42.6.831.
[21] P. Piran Aghl, C.J. Naito, H.R. Riggs, Full-scale experimental study of impact demands resulting from high mass, low velocity debris, J. Struct. Eng. 140 (2014) 04014006, https://doi.org/10.1061/(asce)st.1943-541x.0000948.
[22] A. De Iasio, B. Ghiassi, R. Briganti, G. Milani, Waterborne debris impact forces on wall structures: elastic analytical model integrating the effects of the structural mass, Eng. Struct. 330 (2025) 119928, https://doi.org/10.1016/j.engstruct.2025.119928.
[23] A. De Iasio, B. Ghiassi, R. Briganti, Effects of the structural mass on the waterborne debris impact force, Eng. Struct. 318 (2024) 118719, https://doi.org/10.1016/j.engstruct.2024.118719.
[24] finesoftware.eu, Table of Ultimate Friction Factors for Dissimilar Materials | Influence of Friction between Soil and back of the Structure | Online Help | GEO5, (2023). https://www.finesoftware.eu/help/geo5/en/table-of-ultimate-friction-factors-for-dissimilar-materials-01/ (accessed December 11, 2023).
[25] A.K. Chopra. Dynamics of Structures, 5th Edition, Pearson Education Inc, 2020.
[26] B. Kasal, Wood formation and properties. Mechanical Properties of Wood, Encyclopedia of Forest Sciences (2004) 1815–1828. https://doi.org/10.1016/B0-12-145160-7/00041-7.
[27] L. Jansen, P.A. Korswagen, J.D. Bricker, S. Pasterkamp, K.M. de Bruijn, S.N. Jonkman, Experimental determination of pressure coefficients for flood loading of walls of dutch terraced houses, Eng. Struct. 216 (2020), https://doi.org/10.1016/j.engstruct.2020.110647.
[28] C. Petrone, T. Rossetto, K. Goda, Fragility assessment of a RC structure under tsunami actions via nonlinear static and dynamic analyses, Eng. Struct. 136 (2017) 36–53, https://doi.org/10.1016/j.engstruct.2017.01.013.
[29] EN 1998-1, Eurocode 8: Design of structures for earthquake resistance - Part 1: General rules, seismic actions and rules for buildings, Brussels, 2005. https://eurocodes.jrc.ec.europa.eu/EN-Eurocodes/eurocode-8-design-structures-earthquake-resistance (accessed July 20, 2024).
[30] C.J. Cleveland, C. Morris, Dictionary of Energy, Dictionary of Energy (2014) 1–680. https://doi.org/10.1016/C2009-0-64490-1.
[31] D. Strauch. Classical Mechanics: An Introduction, Springer, Berlin, 2009.
[32] G. Dahlquist. Numerical Methods, Prentice-Hall, Englewood Cliffs, N.J., 1974.
[33] A. Gilat. Numerical Methods for Engineers and Scientists: An Introduction With Applications Using MATLAB, Wiley, Hoboken, N.J., 2008.